Energy 334 (2025) 137805

Contents lists available at ScienceDirect

Energy

journal homepage: www.elsevier.com/locate/energy

Synergistic analysis of a wake galloping piezoelectric energy harvester coupled with a DC interface circuit

Junlei Wang [a], Liangjun Luo [a], Ye Zhang [b], Guobiao Hu [b,*]

[a] School of Mechanical and Power Engineering, Zhengzhou University, Zhengzhou, 450002, China
[b] Internet of Things Thrust, The Hong Kong University of Science and Technology (Guangzhou), Nansha, Guangzhou, Guangdong, 511400, China

ARTICLE INFO

Keywords:
Piezoelectric energy harvesting
Wake galloping aerodynamic force
CFD simulation
Equivalent circuit model
Interface circuits

ABSTRACT

Since wake galloping piezoelectric energy harvesters (WGPEHs) are inherently multi-physics coupled systems, theoretical performance analysis remains challenging due to the disconnect between fluid-structure interaction and circuit-level analysis. This work proposes an innovative equivalent circuit modeling (ECM)-based framework for multi-physics analysis of WGPEHs, offering the flexibility to integrate any interface circuit directly into the simulation. In the proposed approach, the aerodynamic force acting on the WGPEH is first characterized through CFD simulations. The mechanical dynamics are then translated into an equivalent circuit using mechanical-electrical analogies. In this study, a WGPEH based on a tandem cylinder configuration is designed, fabricated, and experimentally tested in a wind tunnel under various conditions. CFD simulations and flow field analysis are performed to characterize the wake galloping aerodynamic force. Based on these results, an equivalent circuit model of the WGPEH is developed and validated by comparing its output with experimental and CFD simulation results. To further demonstrate the flexibility of the approach, a rectifier bridge circuit for AC-DC conversion is incorporated within the ECM framework. The results confirm that this modeling strategy can not only accurately predict the output performance of the WGPEH but also accommodate complex interface circuits. This work provides a new and effective pathway for the comprehensive analysis and design of wake galloping energy harvesters.

1. Introduction

Flow-induced vibrations (FIV) [1,2] are commonly observed in engineering structures subjected to unsteady fluid flows. Among them, vortex-induced vibration (VIV) is one of the most well-known types, extensively studied for its characteristic periodic vortex-shedding mechanism [3,4]. The major limitation of VIV for wind energy harvesting lies in the fact that its large-amplitude response is restricted to the narrow lock-in region. In contrast, galloping, as a typical self-excited vibration, generally occurs in structures with non-circular cross-sections and is characterized by a low cut-in wind speed and large amplitude oscillations over a broad wind speed range. Therefore, it has gained significant attention in recent years for energy harvesting applications [5,6]. Building upon this, wake galloping, a distinct FIV phenomenon induced by tandem bluff bodies, has also drawn increasing research interest [7,8]. In wake galloping, the downstream bluff body is excited by unsteady disturbances in the wake of the upstream one, resulting in a self-excited response similar to conventional galloping. This mechanism integrates vortex-induced disturbances with galloping effects, resulting in complicated nonlinear fluid-structure interactions. Although these dynamics pose great modeling challenges, they present valuable opportunities for designing high-performance energy harvesting systems.

Wake galloping is a common phenomenon in daily life, especially in slender structures like the cables of cable-stayed bridges and the hangers of suspension bridges. It is initiated by the wave flow generated from a leading structure, leading to the vibrations of the downstream structure [9]. Many researchers have conducted analyses and research on the aerodynamic mechanisms of wake galloping [10,11]. B. Dielen et al. [12] discovered two fundamental flow modes of wake galloping around double cylinders, as illustrated in Fig. 1. The first mode, depicted in Fig. 1(a), takes place when the downstream cylinder is fully engulfed within the shear layer of the upstream cylinder. Wind direction or initial amplitude changes can lead to a transition to the second mode (Fig. 1 (b)). The second mode is characterized by strong gap flow and elevated

This article is part of a special issue entitled: CCHVAC2025 published in Energy.

* Corresponding author.
E-mail address: guobiaohu@hkust-gz.edu.cn (G. Hu).

https://doi.org/10.1016/j.energy.2025.137805
Received 20 February 2025; Received in revised form 18 July 2025; Accepted 28 July 2025
Available online 4 August 2025

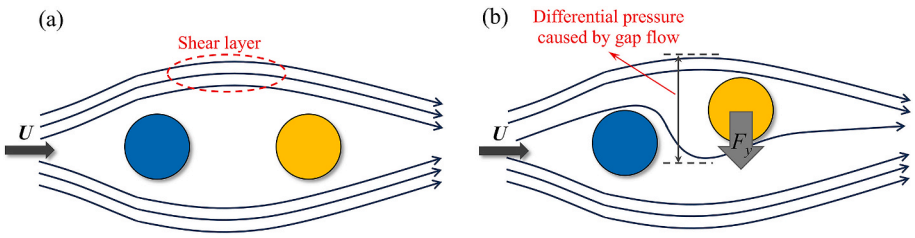

Fig. 1. Two basic flow patterns during wake galloping: (a) Overshoot and (b) Gap flow.

local wind speed around the downstream cylinder, generating a lift force and increasing vibration amplitude. KIM et al. [13] conducted a wind tunnel experiment to study the aerodynamics of closely spaced cables on cable-stayed bridges. They performed flow visualization tests using particle image velocimetry (PIV) and tested various spacing ratios to investigate the characteristics of the wake galloping flow field. Their findings indicate that the spacing ratio is crucial in wake galloping. For small spacing ratios ($L/D = 3.0$–6.0), a distinct galloping phenomenon is observed in the wake, which decreases as the spacing ratio increases. Hirano et al. [14] utilized the Arbitrary Lagrangian-Eulerian (ALE) method within a finite element-based numerical fluid flow analysis. They compared the results with flow visualization data obtained from a smoke-wind tunnel to evaluate the effectiveness of the numerical method. Their findings reveal that the growth in wake galloping amplitude is due to flow transition. As the flow mode shifts from external accelerated flow to gap flow, a vibrational force is generated to amplify the oscillation.

Due to its large vibration amplitude and prolonged duration, wake galloping has traditionally been considered an issue that needs to be mitigated. Yet, with the proposal of a sustainable development strategy, energy problem has become a key challenge to be solved urgently [15–17]. From the perspective of FIV energy harvesting [18–20], it has emerged as a promising renewable energy reservoir that can be harnessed and leveraged [21–23]. Therefore, it has sparked significant enthusiasm among researchers, leading to extensive studies of wake-galloping energy harvesting [24–27]. Usman et al. [28] proposed a wake galloping energy harvester utilizing MFC patches and experimentally investigated how the wind speed and the relative position of the downstream bluff body affect the output voltage. Their results showed that the harvester performs exceptionally well when the wind speed exceeds 4 m/s. Moreover, it was determined that the optimal distance between the upstream and the downstream bluff body is three times the diameter of the upstream bluff body. Zhao et al. [29] employed a D-shaped cylinder as an upstream bluff body and developed a mathematical model of a hydrodynamic energy harvester. They conducted tests in a circulating water channel to validate the model. Jung et al. [30] designed and prototyped an electromagnetic energy harvester that can generate approximately 370 mW when exposed to a wind speed of 4.5 m/s. To conduct a real-world evaluation of the system, particularly in the context of cable-stayed bridges, the authors identified three potential installation sites on the Second Jindo Bridge in South Korea and conducted case studies. The harvested energy was used to power the wireless sensor nodes on the bridge. The research showed that this energy harvester could supply the operation of the sensor nodes for more than 5 days. Du et al. [31] investigated a hybrid energy harvester that combines piezoelectric and electromagnetic techniques to harness wake galloping and finally convert ocean wave energy into electricity. The device comprises a piezoelectric cantilever beam with a bluff body at its free end, an electromagnetic converter enclosed within the bluff body, and an oscillating water column (OWC) wave energy harvesting device. A theoretical model and a multi-physics coupling simulation were developed and established. Experimental testing validated the model, allowing for a quantitative evaluation of offshore energy harvesting efficiency. Liu et al. [32] developed an autonomous nonlinear delay differential equation model to describe wake-induced rotational galloping, explaining the system instability caused by aerodynamic memory effects. Through extensive experiments, they analyzed the influence of various geometric parameters on the system's dynamics and validated the developed model. The experimental results demonstrated that the system achieved an average output power of 9.3 mW at the wind speed of 10 m/s, corresponding to a power density of 131 W/m^3, highlighting its high energy conversion efficiency.

While many studies on wake galloping energy harvesting have concentrated on the mechanical aspects, some researchers have proposed equivalent circuit model (ECM) representations for PEHs [33]. The ECM approach bridges the mechanical and electrical domains, allowing for system-level analyses of these devices [34–36]. Yang et al. [37] built an ECM that incorporated multiple modes to integrate structural modeling with electrical simulation and evaluated various modeling approaches for PEHs. Priore et al. [38] proposed an ECM representation in the Simulink environment to predict and evaluate the performance of an energy harvester based on VIV-galloping interaction. Moreover, they investigated the behaviors of their energy harvester when shunted to the standard AC, DC, and P-SSHI interface circuits. Zhao et al. [39–41] shunted a GPEH to various interface circuits and compared the performance of five interface circuits (SCE, S-SSHI, P-SSHI, DC, and simple AC circuits). They offered suggestions for selecting the most suitable circuit based on factors including wind speed, terminal load, electromechanical coupling strength, and vibration amplitude. For instance, the SCE circuit is recommended for situations with weak coupling and high wind speeds. In 2022, Jia et al. [42] established a typical ECM of a VIVPEH and carried out a comprehensive analysis of its performance shunted to different interface circuits. They found that the optimal power generated from the AC circuit surpassed that of the DC circuit. In 2024, Wang et al. [43] also studied the energy harvesting characteristics of nonlinear VIVPEH connecting AC, DC, and SSHI interface circuits through circuit simulation. The results show that the P-SSHI circuit interface can effectively increase the average output power of the energy harvester by 65.04 % and 174.32 % compared with the AC and DC circuit interfaces. In summary, efforts have been devoted to representing VIVPEHs and GPEHs using equivalent circuits and then shunting to various interface circuits.

However, the development of an equivalent circuit model for WGPEH has not been conducted and completed, mainly due to the intricate fluid-structure coupling characteristics of the wake galloping phenomenon, which pose challenges in accurately constructing its dynamic model. Abdelkefi et al. [44] experimentally investigated the WGPEH connected to a load resistance. They found that the optimal load resistance was approximately 1 MΩ, at which the average harvested power was maximized for the two wind speeds tested. Yang et al. [45] extracted the time history data of the aerodynamic lift force from CFD simulation. Using the energy equivalence principle, they identified the aerodynamic parameters of the unsteady wake galloping forces (UWGF) model. Based on the aerodynamic lift spectrum, they established a nonlinear mathematical model of the UWGF with two sets of cylinders by integrating the self-excited and vortex forces. They subsequently verified the model using experimental results. Despite the outlined endeavors, a comprehensive analysis of the influences of interface circuits

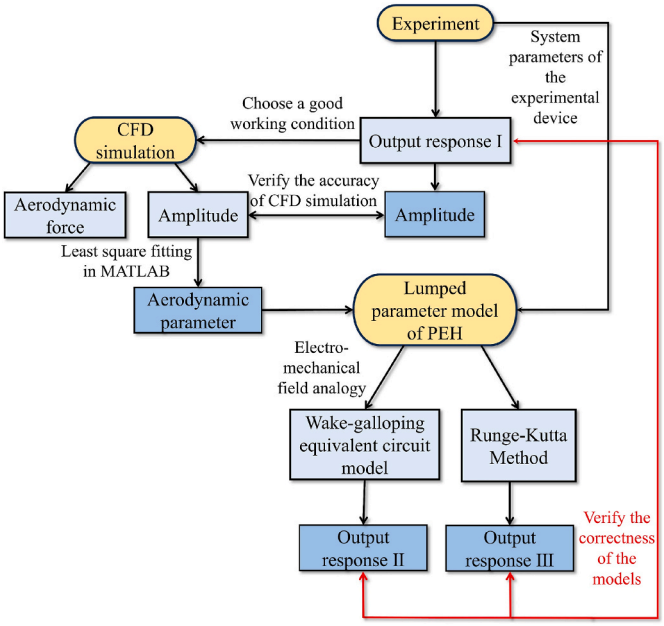

Fig. 2. The flowchart outlining the research methodology employed in this study.

on a WGPEH cannot be conducted without an appropriate equivalent representation.

In this study, the dynamic models of the WGPEH under various experimental conditions are developed through a combination of experiments and CFD simulations. An equivalent circuit model is proposed based on the analogy between the mechanical and electrical domains. The model's accuracy is validated via the comparison with experimental and simulation results, and the effects of different interface circuits on the energy harvesting efficiency are carefully investigated. The research methodology is further elucidated in the flow chart depicted in Fig. 2.

2. Experimental study

The WGPEH prototype used in this study is depicted in Fig. 3(a). The frame is made of industrial aluminum. The piezoelectric sheet used in the experiments was a commercially available piezoelectric ceramic material (PZT-5), with dimensions of 30 × 20 × 0.4 mm^3. Its piezoelectric constants are $d_{31} = -185 \times 10^{-12}$ C/N and $d_{33} = 400 \times 10^{-12}$ C/N. In addition, Young's modulus is 60 GPa, and Poisson's ratio is 0.36. It was affixed near the clamped end of the cantilever beam using acrylate adhesive. The other end is attached to a cylindrical bluff body in a 'T' configuration. The bluff body and the cantilever beam are made of foam and aluminum, respectively. Moreover, in the direction of incoming flow, a first cylindrical bluff body, referred to as the upstream interference cylinder, is mounted on the same frame via a stainless steel tube. The upstream cylinder has the same shape and size as the downstream counterpart. The top surfaces of both cylinders align with the direction of the incoming wind, and the distance between their centers is denoted

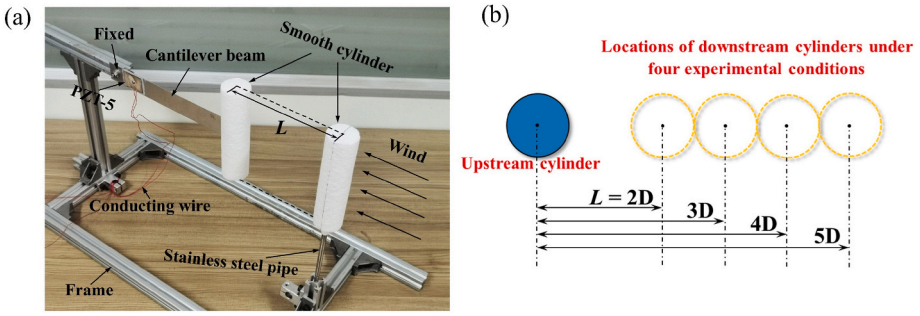

Fig. 3. (a) Physical prototype of the Wake Galloping Piezoelectric Energy Harvester (WGPEH). (b) Investigation of the positioning of the downstream cylinder in relation to the upstream cylinder under four experimental conditions.

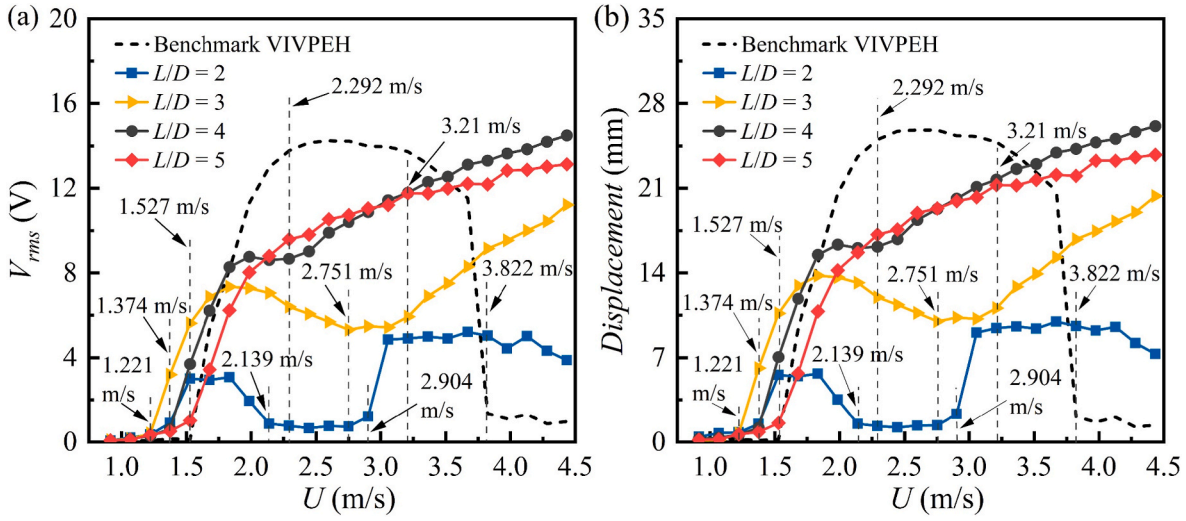

Fig. 4. Output responses of the WGPEHs with different *L/D* ratios: (a) RMS open circuit voltage versus wind speed; (b) Tip displacement versus wind speed.

Table 1
System parameters of the prototyped WGPEH.

System parameter	Symbol	Value	Unit
Effective mass	M_{eff}	3.67×10^{-3}	Kg
Effective stiffness	K_{eff}	12.572	N/m
Damping ratio	ξ	0.011	/
Effective damping	C_{eff}	0.048	N·s/m
Open-circuit natural frequency	f_{on}	9.313	Hz
Short-circuit natural frequency	f_{sn}	9.278	Hz
Air density	ρ	1.204	Kg/m^3
Piezoelectric capacitance	C_p	41.782	nF
Electromechanical coupling coefficient	θ	2×10^{-5}	N/V

as L. The dimensions of the cylinders are $D \times H = 31 \times 120$ mm^2, where D is the characteristic length, and H is the height of the bluff body. The cantilever beam measures $L_b \times B_b \times T_b = 200 \times 25 \times 0.5$ mm^3 and the piezoelectric patch measures $L_p \times B_p \times T_p = 30 \times 20 \times 0.4$ mm^3, L, B, and T represent length, width, and thickness, respectively. The subscripts b and p indicate the beam and piezoelectric patch, respectively. Many studies have shown that the spacing ratio is a critical factor that affects wake galloping. Consequently, this study examines a spacing ratio ranging from 2D to 5D. Fig. 3(b) illustrates the positioning of the downstream cylinder.

During the experiment, the entire setup, including the WGPEH prototype, is placed in an open-circuit wind tunnel made of plexiglass, with a diameter of 400 mm and a length of 5 m. The whole wind tunnel can be roughly divided into the entrance and testing sections. Air enters the wind tunnel through a gradually narrowing entrance, initially causing turbulence. Four honeycomb structures then condition this turbulent flow to achieve a uniform and steady airflow. The WGPEH prototype is positioned in the testing section, where it undergoes testing under a stable incoming flow. The wind speed tuning is achieved by controlling the frequency modulator. The frequency modulation range is 0–50 Hz, and the conversion relationship between wind speed and frequency is $U = 0.153f + 0.15$. The natural frequency f_n of the WGPEH is identified through a free attenuation experiment. It is important to note that f_n aligns with the natural frequency of the benchmark VIVPEH after removing the upstream cylinder. As the incoming air flows towards the WGPEH, it initially encounters the upstream fixed cylinder, resulting in periodic vortex shedding and forming a vortex street. Consequently, the downstream cylinder is not exposed to a stable incoming flow but rather to the wake generated by the vortex shedding of the upstream cylinder. When the vortex shedding frequency approximates f_n, the downstream bluff body vibrates in concert with the cantilever beam, causing the piezoelectric patch to deform and generate a voltage output. The electrodes of the piezoelectric patch are connected to a digital oscilloscope (ISDS220B) via wires for measuring and recording voltage outputs, and the bluff body displacement is gauged using a laser sensor. The tunable wind speed range in the experiment is 0.915 m/s ~4.434 m/s. In our study, the upper wind speed limit of 4.5 m/s was chosen after careful consideration. For the benchmark VIVPEH, this wind speed lies outside its lock-in region, and preliminary studies indicated it is an appropriate upper limit for testing the system's response. The data shown in Fig. 4, which covers the wind speed range below 4.5 m/s, sufficiently captures the dynamic characteristics of the wind energy harvesters, including the cut-in, growth, and transition to the saturation phase. This range provides adequate information for analyzing and comparing their behavior and energy harvesting potential. Moreover, previous studies [46,47] have demonstrated that beyond a certain wind speed, the growth rate of the response amplitude significantly decreases. As wind energy harvesters are specifically designed to operate efficiently at low wind speeds, investigating the system's behavior at higher wind speeds is not deemed necessary for the objectives of this study. Table 1 shows the system parameters of WGPEH.

For different spacing ratios, the displacements of the bluff body and the voltage outputs at various wind speeds are experimentally measured and presented in Fig. 4. The results of the benchmark VIVPEH without the upstream cylinder are also included for comparison. The dashed line (benchmark VIVPEH) illustrates typical vortex-induced vibration (VIV) characteristics, with a cut-in wind speed of 1.527 m/s. With the wind speed range of 1.527–3.822 m/s, the vortex shedding frequency behind the upstream cylinder aligns with the natural frequency of the downstream harvester, resulting in periodic oscillations within the lock-in region. This phenomenon is beneficial to energy harvesting.

Subsequently, the experimental results for four different spacing ratios, as presented in Fig. 4, reveal three distinct response characteristics [48]: decoupled VIV and WG (wake galloping), coupled VIV and WG, and pure WG. Specifically, the tandem cylinder system exhibits the following behavior. At low wind speeds, the downstream cylinder primarily responds to periodic excitations induced by vortex shedding from the upstream cylinder, resulting in a typical VIV-dominated response. As the wind speed U increases, the instability of wake shear layers intensifies, modulating the aerodynamic force response. This results in the development of negative aerodynamic damping and the onset of self-excited vibration, eventually triggering large-amplitude wake galloping. When $L/D = 2$, the system exhibits a response with VIV and WG clearly separated. In the first regime, over the wind speed range of 1.374–2.139 m/s, the system presents typical VIV characteristics: a pronounced frequency-locking phenomenon, with the vibration amplitude initially increasing and then decreasing. Due to the small spacing, the upstream wake remains relatively stable, and the shear layer development is constrained, thereby suppressing the triggering conditions for WG. As a result, vibrations almost cease beyond the first vibration zone, and the output voltage of the energy harvester remains low. As the wind speed increases to 2.904 m/s, the instability of the wake shear layer intensifies, and the system enters a second vibration regime characterized by typical WG behavior. For $L/D = 3$, the downstream cylinder starts vibrating at 1.221 m/s, and the vibration response exhibits a coupled VIV-WG mode. In the initial stage, VIV dominates, and the vibration amplitude increases with rising wind speed. In the intermediate stage, VIV enters the decay region, resulting in a noticeable amplitude "depression", followed by a rapid increase. This "depression" is caused by a shift in the dominant response mechanism: residual oscillations from decaying VIV enhance shear layer instability, which subsequently triggers WG driven by negative aerodynamic damping. In the final stage, the vibration mode transitions to WG, characterized by a monotonically increasing large-amplitude response. When L/$D = 4$, the response trend is similar to that of $L/D = 3$. A transition between VIV and WG is also observed, accompanied by a "depression" in amplitude; however, the amplitude drop is smaller, and the transition is more gradual. This is because the larger spacing allows the shear layer to exert a stronger modulation effect, accelerating the development of negative aerodynamic damping and the onset of WG, resulting in a smoother transition between the two mechanisms. At $L/D = 5$, the downstream cylinder begins to vibrate at 1.527 m/s, nearly matching the cut-in wind speed of the benchmark VIVPEH. In this case, the response curve exhibits no pronounced "protrusions" or "depressions", and the amplitude increases monotonically with the wind speed. This behavior is primarily attributed to the substantial dissipation of the upstream wake structure at large spacing, which eliminates a stable periodic excitation and hinders the establishment of VIV. As the wind speed increases, asymmetric shear disturbances become more pronounced, causing the system to transition directly into a WG-dominated response. Consequently, the vibration continues to grow steadily with increasing wind speed.

As shown in Fig. 4, we can see that the output voltage of the benchmark VIVPEH first increases once the wind speed exceeds the cut-in speed of 1.527 m/s, but then decreases to almost 0 at 3.822 m/s. When the spacing ratio is 4, the cut-in speed of the WGPEH reduces to 1.374 m/s, and the output voltage monotonically increases after the cut-in speed, without showing a decreasing trend. Compared to the benchmark VIVPEH, the WGPEH can operate at lower wind speeds and maintain functionality over a broader operational bandwidth. From the

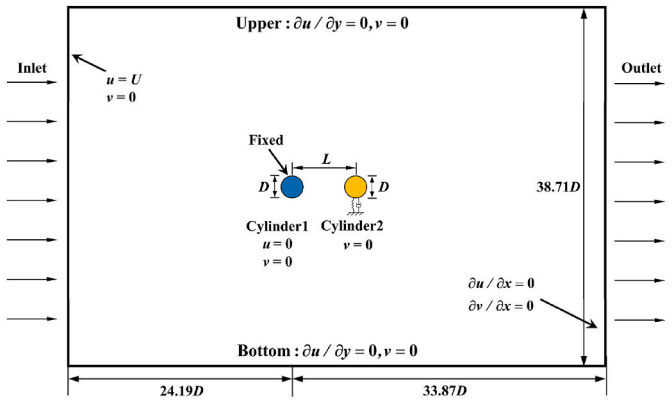

Fig. 5. Computational domains and boundary conditions for the CFD simulation.

above aspects, the energy harvesting performance of the WGPEH is significantly superior to that of the benchmark VIVPEH. This occurs because the upstream wake structure remains highly ordered with minimal energy loss, allowing the downstream cylinder to continuously harness energy from the upstream wake, even if the wind speed increases, thereby sustaining or enhancing its vibration. However, the energy harvesting efficiency varies across different spacing ratios because optimal matching between wake disturbances and the cylinder's dynamic response plays a crucial role in maximizing energy transfer. As the spacing ratio increases from 2 to 4, the voltage and amplitude under the same wind speed almost consistently increase. However, when the spacing ratio is increased to 5, the voltage and amplitude values within the wind speed range of 0.915 m/s to 4.434 m/s exhibit slight decreases compared to those observed with a spacing ratio of $L/D = 4$. Moreover, the change rate of the output voltage over the wind speed range of 3.21 m/s to 4.434 m/s is greater for $L/D = 4$ than for $L/D = 5$. From the above results, we can conclude that when wind speed exceeds 4.434 m/s, the energy harvesting efficiency of the WGPEH with $L/D = 4$ outperforms that of $L/D = 5$. In addition, if the spacing ratio increases beyond 5, although this study does not include experimental investigations for this range, previous studies [46,49] have shown that with further increases in the spacing ratio, the wake tends to act like a free flow field, weakening the WG mechanism and resulting in a decrease in the vibration amplitude of the downstream cylinder. Therefore, the optimal output effect is achieved with a spacing ratio of 4, leading to the selection of $L/D = 4$ for the following simulations.

3. CFD simulation

3.1. CFD model

Two-dimensional CFD simulations of the WGPEH were performed using XFlow, which utilizes the Lattice Boltzmann Method (LBM) [50]. XFlow is particularly well-suited for solving complex fluid-structure interaction problems, as it can efficiently and accurately simulate unsteady flow phenomena, such as vortex shedding, without the need for complex mesh generation. Fig. 5 shows the calculation domain and boundary conditions. The dimensions of the calculation domain are $58.06D \times 38.71D$. The distance from the center of the upstream cylinder to the velocity inlet on the left side is $24.19D$, and the distance to the flow outlet on the right side is $33.87D$. The longitudinal blocking rate is determined to be $D/38.71D = 2.58$ %, which is less than the 6 % limit specified in Ref. [51] and thus meets the calculation requirements. Both the upper and lower boundaries are set as fixed walls. The upstream cylinder is fixed, and the center-to-center distance between the two cylinders is $L = 4D$. Due to the fluid forces, the downstream cylinder may undergo lateral movement.

Before proceeding to the aerodynamic analysis of the proposed WGPEH, we will first present a convergence verification because prioritizing convergence verification is crucial to upholding the accuracy and reliability of numerical simulations. Given the substantial influences of fluid flow conditions at different wind speeds on lattice independence verification, high wind speed simulations require greater lattice precision. Therefore, a tandem double-cylinder model with a wind speed of $U = 4.5$ m/s is selected for lattice independence verification to ensure that the lattice division is applicable for wind speeds between 0.915 m/s and 4.434 m/s. The incoming air properties are as follows: mass density of 1.204 kg/m^3, thermal conductivity of 0.0243 W/(m·K), heat capacity of 1006.43 J/(kg·K), molecular weight of 28.99 g/mol, and dynamic viscosity of 1.7894×10^{-5} Pa s.

At the entrance of the tandem double-cylinder model, a uniform wind speed of $U = 4.5$ m/s results in a Reynolds number of 9387.05, indicating turbulent flow. Within the turbulent regime, the motion of the fluid flow demonstrates notable unpredictability. Therefore, the Smagorinsky model in XFlow is applied to simulate the turbulence. This model can accurately predict the formation and destruction of small and medium-sized vortices within the turbulent flow [52]. Since vortex shedding between and behind the two cylinders primarily influences the motion of the downstream cylinder, areas with large vortex shedding around and behind the cylinders are selected for lattice refinement. Fig. 6 shows the lattice of the calculation domain along with a close-up view. A finer lattice is concentrated around the bluff body to precisely simulate the boundary layer, with a resolution 16 times higher than that of the overall lattice. To further ensure lattice accuracy, three different

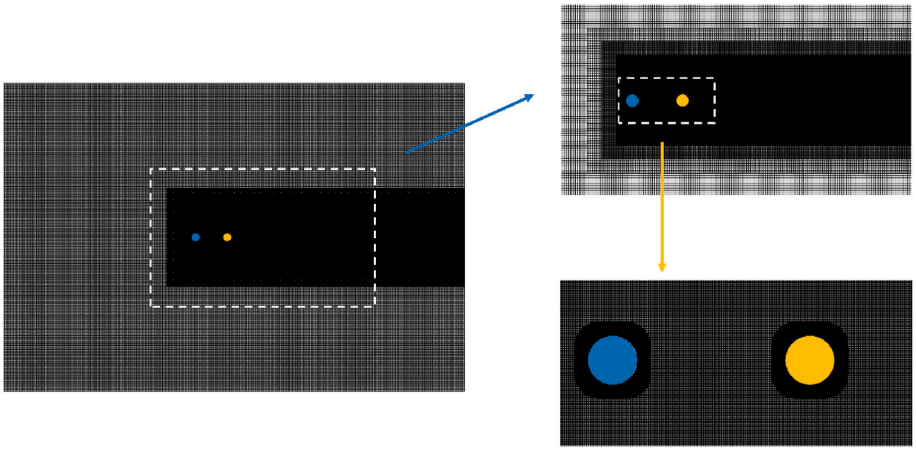

Fig. 6. Computational lattice and local lattice around the upstream and downstream cylinders.

Table 2
Lattice independence verification. The relative errors are included in the parentheses starting from the second row.

Resolution	Lattice number	Upstream cylinder		Downstream cylinder		
		C_{Dmean}	C_{Lrms}	C_{Dmean}	C_{Lrms}	*Displacement*
Rough	502,600	1.796	1.269	0.662	0.752	25.669 mm
Medium	649,644	1.733 (3.51 %)	1.259 (0.79 %)	0.873 (24.17 %)	0.757 (0.66 %)	25.410 mm (1.01 %)
Fine	865,382	1.725 (0.46 %)	1.244 (1.19 %)	0.822 (5.84 %)	0.713 (5.81 %)	25.043 mm (1.44 %)

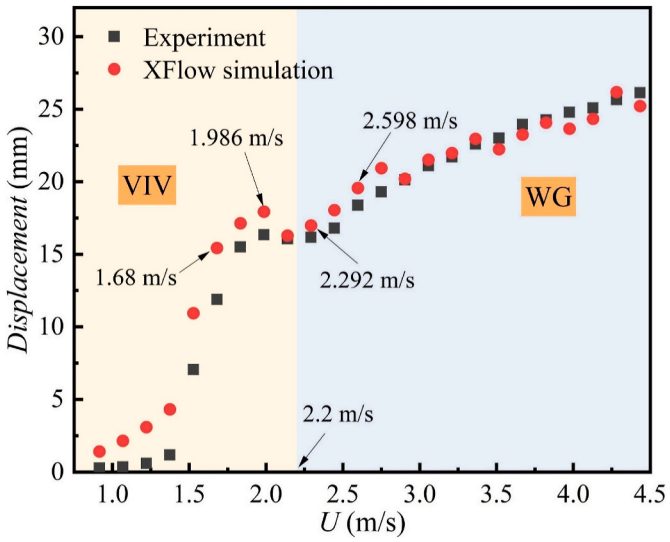

Fig. 7. Displacement amplitude of the WGPEH versus wind speed: red dots – simulation results; black squares – experimental results.

resolutions, i.e., rough, medium, and fine, are evaluated, with corresponding lattice cell counts of 502,600, 649,644, and 865,382. To strike a balance between calculation accuracy and efficiency, the "time step mode" in XFlow is set to "Fixed-Automatic," utilizing an adaptive time step to accommodate the refined grid and maintain the software's stability parameter below 0.3.

The drag coefficient C_D and lift coefficient C_L of the two cylinders are extracted, as well as the displacement of the downstream cylinder. The coefficients are defined as $C_D = F_D/(0.5\rho U^2 DH)$, $C_L = F_L/(0.5\rho U^2 DH)$, where F_D and F_L represent the drag and lift forces, respectively, obtained by integrating the pressure and friction along the surfaces of the cylinders. The mean drag coefficient C_{Dmean}, the RMS lift coefficient C_{Lrms}, and the displacement of the downstream cylinder obtained using different lattice resolutions are listed in Table 2. The lattice resolution steadily enhances from rough to fine, with the associated changes in the dimensionless fluid force coefficients and displacements indicated in parentheses. The results reveal that the discrepancy between the numerical results for the two cylinders is below 6 % at medium and high-resolution lattice sizes, satisfying convergence criteria for engineering applications. Therefore, in light of both accuracy and efficiency considerations, the medium-resolution lattice size is selected for the following CFD simulations.

3.2. Simulation results

Fig. 7 shows the displacement amplitude of the downstream cylinder versus the wind speed for $L/D = 4$. The black squares represent experimental data; the red dots represent the CFD simulation results. It can be observed that when the wind speed is lower than 1.833 m/s, the amplitude obtained from the CFD simulation is significantly larger than that from the experiment. The primary reason for this discrepancy is that, during the early stage, the cantilever beam suppresses vortex formation, leading to a corresponding reduction in the vibration amplitude of the bluff body in the VIV stage [53]. However, these practical factors are not considered in the CFD simulation, leading to a noticeable discrepancy between the two when $U < 1.833$ m/s. When the wind speed reaches or exceeds 1.833 m/s, the amplitude of the bluff body in both the simulation and experiment shows high consistency at the same wind speed, with a maximum relative error of 10.55 %. The relative error was calculated by taking the difference between the peak amplitudes of the simulation and experimental results obtained under the same conditions. This validates the accuracy of the XFlow numerical simulation and further confirms the reliability of the extracted aerodynamic parameters. In Fig. 7, the WGPEH exhibits VIV output characteristics at wind speeds below 2.2 m/s and transitions to WG above this threshold. To investigate the transition from VIV to WG, four wind speed points are selected at 1.68 m/s, 1.986 m/s, 2.292 m/s, and 2.598 m/s. The flow field variations across these four working conditions are analyzed to uncover the underlying mechanism.

Firstly, from the perspective of the flow field, this study investigates

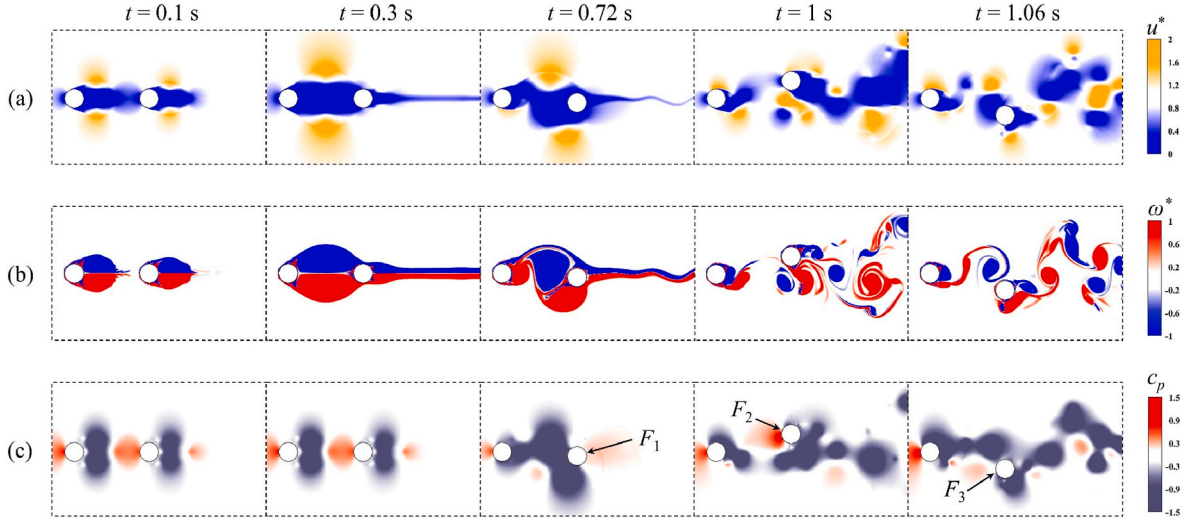

Fig. 8. Contours of the flow field at the wind speed of 2.598 m/s: (a) Velocity field; (b) Vorticity field; (c) Pressure field.

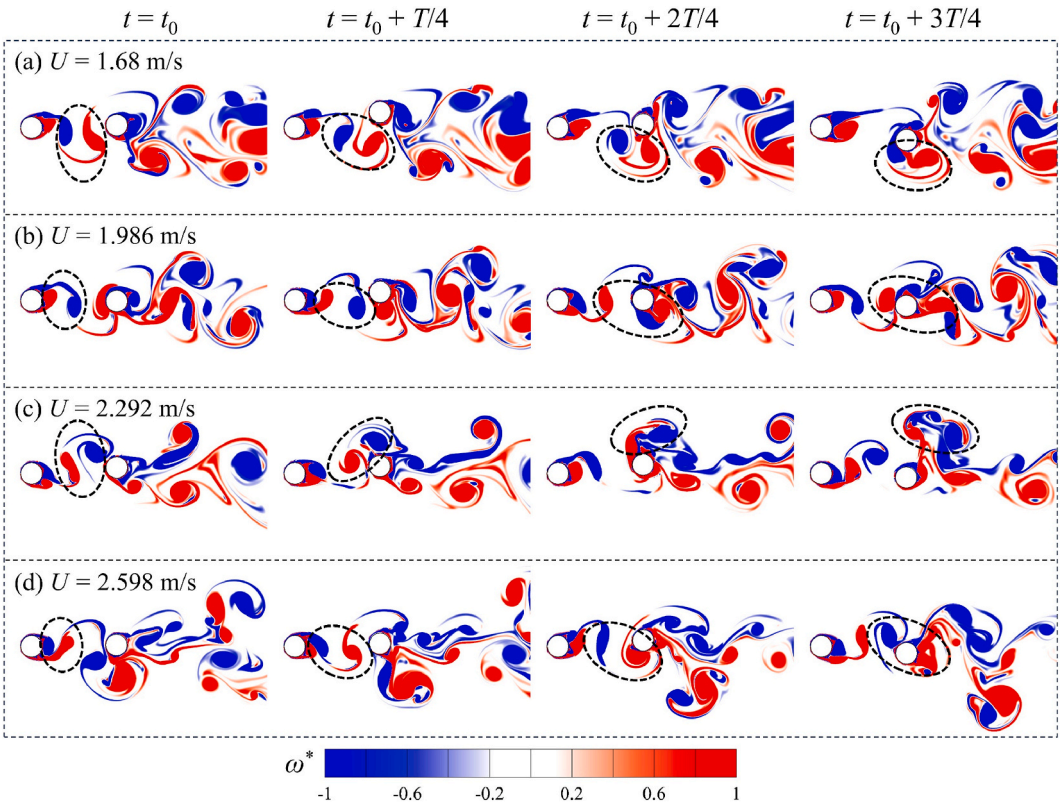

Fig. 9. Vorticity contours around the tandem cylinders in one period at different wind speeds.

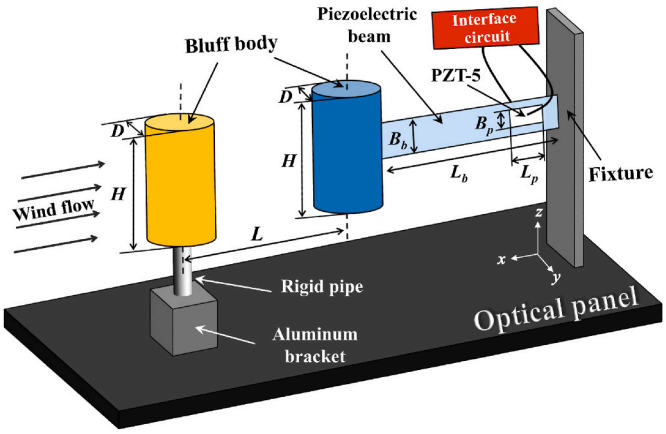

Fig. 10. Mechanical configuration of the WGPEH.

how the wake of the upstream cylinder causes the vibration of the downstream cylinder. Fig. 8 presents the two-dimensional flow field diagrams for $U = 2.598$ m/s, showcasing the transition from the static state to the initiation vibration of the downstream cylinder. These diagrams, obtained using Tecplot (a software tool for data visualization), include the velocity field (Fig. 8(a)), the vorticity field (Fig. 8(b)), and the pressure field (Fig. 8(c)). $u^* = u/U$ is defined to denote the dimensionless velocity; the dimensionless vorticity ω^* ranges from -1 to 1; and $c_p = 2P_{static}/(\rho U^2)$ represents the pressure coefficient, where u is the instantaneous velocity at different positions, U is the inlet velocity of the incoming flow, P_{static} is the local static pressure, and ρ is the fluid density. At $t = 0.1$ s, the incoming fluid starts to interact with the upstream cylinder, forming a low-speed, high-pressure region in front of it and a pair of positive and negative vortices behind it. At $t = 0.3$ s, the low-speed region between the two cylinders widens, leading to accelerated airflow on both sides and the formation of two symmetrical high-speed zones. The positive and negative vortices behind the upstream cylinder become larger, forming an area that almost wraps the two cylinders. The cylinders remain stationary at this stage, and the pressure distribution resembles that observed at $t = 0.1$ s. At $t = 0.72$ s, the negative vorticity between the two cylinders begins to rotate clockwise, and the positive one rotates counterclockwise. As a result, the two previously symmetrical high-speed regions undergo a deflection, causing changes in the pressure distribution. In the CFD simulation, we consider only the motion of the downstream cylinder in the y-direction. Unlike the horizontal pressure distributions observed at previous time instants, at $t = 0.72$ s, the downstream cylinder experiences a force F_1 directed towards the lower left, as illustrated in the third column of Fig. 8. This force is expected to drive the cylinder to move downward. At $t = 1$ s and 1.06 s, the regular vorticity shed by the upstream cylinder is dispersed by the downstream cylinder, resulting in an irregular high-speed region. As shown in the last two columns of Fig. 8, high-pressure regions occasionally form in front of the downstream cylinder, resulting in varying applied forces of F_2 and F_3 on the cylinder. Consequently, the alternating nature of these forces causes the downstream cylinder to oscillate periodically in the y-direction.

A two-dimensional vorticity diagram of the tandem double cylinders with a spacing ratio of 4 is obtained by CFD simulation and shown in Fig. 9. Vibrations at four specific time instants, evenly spaced throughout a period duration, have been chosen to illustrate the complete vibration process. At $U = 2.292$ m/s, the vortex shedding area of the tandem cylinder in the y-direction is smaller than in other cases. The results indicate that the energy carried in the wake of the upstream cylinder reduces, resulting in a decrease in the excitation force on the downstream cylinder and, thus, a weakened vibration amplitude. These findings align well with our analysis in section 2. Fig. 9 shows the trajectory of a pair of vortices shedding from the upstream cylinder over one cycle, each highlighted at four different wind speeds. The shedding of positive and negative vortices from the upstream cylinder affects the

downstream cylinder, leading to the oscillation of the downstream cylinder. As the vortices move, they gradually merge with the vortex field around the downstream cylinder, forming larger vortices. The intensified vortices produce significant pressure contrast between the upper and lower surfaces of the downstream cylinder, boosting the vibration of the downstream cylinder and enhancing the energy harvesting performance.

4. Equivalent circuit model

4.1. Lumped parameter modeling

Fig. 10 depicts the geometric model of the WGPEH. It consists of two cylinder bluff bodies, a cantilever beam, and a piezoelectric sheet. Building upon conventional VIVPEH concepts, the wake galloping model explored in this study is achieved by introducing an upstream interference bluff body secured by a steel pipe in front of the downstream harvester. The steel pipe and the upstream bluff body form a configuration resembling the numeral "1". The two cylinders have the same characteristic length denoted as D. As the wind speed rises, the upstream bluff body remains stationary since it is fixed on the rigid pipe. However, its existence disrupts the previously stable airflow, introducing chaos. When the eddy detachment excitation of the downstream bluff body surpasses a critical threshold, periodic oscillations in the y-direction become evident.

A PEH can be modeled as a combination of a current source $I(t)$ and a capacitor C_p connected in parallel. When shunted to a load resistor R_L, the current $I(t)$ splits between the capacitor C_p and the resistor R_L. Assuming the voltage across the piezoelectric transducer is $V(t)$, the current flowing through the resistor is $V(t)/R_L$, and the current flowing into the capacitor is $C_p{\cdot}dV(t)/dt$. According to Kirchhoff's current law:

$$I(t)=\frac{V(t)}{R_L}+C_p.\frac{dV(t)}{dt} \tag{1}$$

According to the piezoelectric coupling principle, the total current $I(t)$ generated by the PEH is proportional to the mechanical velocity [54]. Based on Euler-Bernoulli beam theory, one can then derive the second-order differential equations for cantilever beams with piezoelectric layers. When an energy harvester vibrates primarily around its fundamental mode, it can be simplified to a single-degree-of-freedom (SDOF) model. Hence, under the assumption of considering only the fundamental mode, the governing equation can be written as:

$$\begin{cases}\ddot{\eta}(t)+2\xi\omega_n\dot{\eta}(t)+\omega_n^2\eta(t)+\chi V(t)=F_{wg}(t)\\ V(t)/R_L+C_p\dot{V}(t)-\chi\dot{\eta}(t)=0\end{cases} \tag{2}$$

where $F_{wg}(t)$ is the wake galloping aerodynamic force, the term on the right-hand side of the second equation in equation (1) corresponds to the mechanical velocity, $\eta(t)$ represents the fundamental modal coordinate, $\dot{\eta}(t)$ and $\ddot{\eta}(t)$ are modal velocity and modal acceleration, respectively. ξ is the damping ratio, and ω_n is the natural frequency, which can be generally identified via a free decay test, χ represents the modal coupling coefficient, $V(t)$ denotes the voltage across the load resistance.

By defining the lumped parameters $M_{eff}=1/\varphi^2(L_b)$, $C_{eff}=2\xi\omega_n/\varphi^2(L_b)$, $K_{eff}=\omega_n^2/\varphi^2(L_b)$, $\theta=\chi/\varphi(L_b)$, $y(L_b,t)=\varphi^2(L_b)\eta(t)$, one can eliminate the mode terms and transform the governing equations into:

$$\begin{cases}M_{eff}\ddot{y}(L_b,t)+C_{eff}\dot{y}(L_b,t)+K_{eff}y(L_b,t)+\theta V(t)=F_{wg}(t)\\ V(t)/R_L+C_p\dot{V}(t)-\theta\dot{y}(L_b,t)=0\end{cases} \tag{3}$$

where M_{eff} is the equivalent mass, $M_{eff}=33/140m_1+m_2$, with m_1 being the mass of the cantilever beam and m_2 the tip mass attached at the free end, i.e., the mass of the bluff body in our case. $y(L_b,t)$ denotes the displacement of the bluff body; C_{eff} is the equivalent damping coefficient, $C_{eff}=2\xi\omega_nM_{eff}$, ξ is the damping ratio; $K_{eff}=\omega_n^2M_{eff}$ is the equivalent stiffness; θ is the electromechanical coupling coefficient, which indicates the capability of the piezoelectric element to convert mechanical energy into electrical energy; C_p is the capacitance of the piezoelectric patch; R_L is the load resistance. These equivalent lumped parameters can be derived using the mode decomposition method, assuming the dominance of the fundamental mode [55,56]. Alternatively, they can be identified in the experiment [57,58]. In this study, the latter method was employed to determine the lumped parameters, as it provides a more accurate representation in practical applications, where many realistic factors can not be fully considered by the theoretical model. The equivalent lumped parameters identified for the system in this study are listed in Table 1. $F_{wg}(t)$ is the total aerodynamic force applied on the downstream bluff body. To predict and describe this force, this study utilizes an unsteady model [45] that, despite being computationally intricate, offers a comprehensive representation of the unsteady features inherent in the fluid-structure interaction system.

In this model, the aerodynamic force is divided into two components: the self-excited force and the vortex-excited force. For brevity, $y(L_b,t)$ and $\dot{y}(L_b,t)$ will be denoted as y and $\dot{y}$, respectively.

$$F_{wg}(t)=F_{se}(y,\dot{y})+\sum_{i=1}^{n}F_{vi}(f_{si}) \tag{4}$$

where $F_{se}(y,\dot{y})$ and $\sum_{i=1}^{n}F_{vi}(f_{si})$ are self-excited force and vortex-excited forces respectively. By performing higher-order Taylor sequence expansion for y and $\dot{y}$, the self-excited force can be expanded into a polynomial form. In analogy to an equivalent linear system, the self-excited force is further divided into aerodynamic damping force, aerodynamic stiffness force, and aerodynamic pure force terms, as below:

$$\begin{aligned}F_{se}(y,\dot{y})=&\underbrace{g_{01}\dot{y}+g_{03}\dot{y}^3+g_{05}\dot{y}^5}_{\text{aerodynamic damping force}}+\underbrace{g_{10}y+g_{30}y^3+g_{50}y^5}_{\text{aerodynamic stiffness force}}\\&+\underbrace{g_{11}\dot{y}y+g_{22}y^2\dot{y}^2+g_{04}\dot{y}^4}_{\text{aerodynamic pure force}}\end{aligned} \tag{5}$$

Considering that the work contributed by the pure force terms and stiffness force terms is much smaller than the work done by the aerodynamic damping terms [59] and their impact on the WG vibration amplitude is less than 1 % [60,61], the aerodynamic force in wake galloping is therefore deemed primarily governed by velocity-dependent terms [61]. We have prioritized retaining them in the modeling to highlight the self-excited mechanism driven by nonlinear damping. The omission of the displacement term is a simplification aimed at streamlining the parameter identification process. Therefore, when focusing on the stable or the predicted amplitude, it suffices to consider the aerodynamic damping forces only. Hence, equation (5) can be simplified as:

$$F_{se}(y,\dot{y})=g_{01}\dot{y}+g_{03}\dot{y}^3+g_{05}\dot{y}^5 \tag{6}$$

where g_{ij} are numerical parameters, which can be obtained by numerical calculation.

For the vortex-induced force $\sum_{i=1}^{n}F_{vi}(f_{si})$, it is a function of the vortex shedding frequency. During wake galloping, the flow of fluid passing the upstream cylinder creates distinct flow lines behind the cylinder due to the flow-blocking effect, ultimately causing the formation of vortices. Periodically detaching from the upstream cylinder and traveling downstream, these vortices affect the downstream cylinder by striking its surface and altering the surrounding pressure, ultimately resulting in its vibration. The vortex shedding of the upstream cylinder affects not only its own vibration but also the vortex shedding mode of the downstream cylinder. Therefore, the vortex-induced force is related to the

vortex-off frequency (f_{s1}) of the upstream cylinder and that of the downstream cylinder (f_{s2}). Thus, $\sum_{i=1}^{n} F_{vi}(f_{si})$ can also be expressed as $F_{vi}(f_{s1}, f_{s2})$, which can be expressed as follows:

$$F_{vi}(f_{s1}, f_{s2}) = v_1 \sin(2\pi f_{s1} t + \varphi_1) + v_2 \sin(2\pi f_{s2} t + \varphi_2) \tag{7}$$

$f_{si} = S_{ti}U/D$, where D is the diameter of the bluff body, U is the wind speed, and S_{ti} is the Strouhal number, which is often employed in analyzing vortex shedding frequency. f_{si} in equation (7) can be expressed by S_{ti} as follows:

$$F_{vi}(f_{s1}, f_{s2}) = v_1 \sin(2\pi t S_{t1} U / D + \varphi_1) + v_2 \sin(2\pi t S_{t2} U / D + \varphi_2) \tag{8}$$

Among them, the phase angles φ_1 and φ_2 are two parameters that need to be fitted. To facilitate the aerodynamic force solution, equation (8) is changed to:

$$\begin{aligned} F_{vi}(f_{s1}, f_{s2}) = {} & v_{11} \sin(2\pi t S_{t1} U/D) + v_{12} \cos(2\pi t S_{t2} U/D) \\ & + v_{21} \sin(2\pi t S_{t2} U/D) + v_{22} \cos(2\pi t S_{t2} U/D) \end{aligned} \tag{9}$$

By substituting equations (6) and (9) into equation (4), the wake galloping force considering only the stable amplitude can be expressed as follows:

$$\begin{aligned} F_{wg}(t) = {} & g_{01}\dot{y} + g_{03}\dot{y}^3 + g_{05}\dot{y}^5 + v_{11} \sin(2\pi t S_{t1} U/D) + \\ & v_{12} \cos(2\pi t S_{t2} U/D) + v_{21} \sin(2\pi t S_{t2} U/D) + v_{22} \cos(2\pi t S_{t2} U/D) \end{aligned} \tag{10}$$

It is worth noting that the time-dependent term included in equation (10) is primarily used to capture the vortex-induced triggering mechanism, while the core dynamics of the system remain dominated by the self-excited term. This coupled modeling approach has been widely applied in simulating wake galloping phenomena [46,47]. Where g_{01}, g_{03}, and g_{05} represent the first-, thrid-, and fifth-order aerodynamic damping coefficients, respectively. v_{11} and v_{12} are the coefficients of the vorticity-induced force resulting from the vortex detachment of the upstream cylinder, and v_{21} and v_{22} are the coefficients of the vorticity-induced force resulting from the vortex detachment of the downstream cylinder. Taking into account all of the above assumptions, the governing equation of the WGPEH can be obtained as follows:

$$\begin{cases} \left\{ \begin{aligned} & M_{eff}\ddot{y}(t) + C_{eff}\dot{y}(t) + K_{eff}y(t) + \theta V(t) = g_{01}\dot{y}(t) + g_{03}\dot{y}(t)^3 + g_{05}\dot{y}(t)^5 + \\ & v_{11} \sin(2\pi t S_{t1} U/D) + v_{12} \cos(2\pi t S_{t1} U/D) + v_{21} \sin(2\pi t S_{t2} U/D) + v_{22} \cos(2\pi t S_{t2} U/D) \end{aligned} \right\} \\ V(t)/R_L + C_p \dot{V}(t) - \theta \dot{y}(t) = 0 \end{cases} \tag{11}$$

Table 3
Analogies between mechanical and electrical quantities.

Mechanical variables/components	Electrical variables/components
Force: F	Voltage: V
Displacement: $y(L_b, t)$	Charge: $q(t)$
Velocity: $\dot{y}(L_b, t)$	Current: $\dot{q}(t)$
Acceleration: $\ddot{y}(t)$	Rate of current change: $\ddot{q}(t)$
Effective damping: C_{eff}	Resistance: R
Effective mass: M_{eff}	Inductance: L
Reciprocal of effective stiffness: $1/K_{eff}$	Capacitance: C
Electromechanical coupling coefficient: θ	Ideal transformer turn ratio: N

4.2. Equivalent circuit representation

The output generated by the WGPEH is in the form of alternating current (AC) and requires conversion to direct current (DC) for practical purposes. To achieve this AC-DC conversion, a rectifier bridge must be added before the resistive load R_L in equation (11). The nonlinear nature of the rectifier bridge adds additional complexity, making it challenging to obtain analytical solutions. Hence, an equivalent circuit model (ECM) for WGPEH is proposed to address the limitations of traditional methods, which are less effective or even impossible for simulating complex nonlinear circuits. The mechanical system is represented using equivalent electrical elements by leveraging electromechanical analogies. For example, the mechanical equation $F = M\ddot{y}$ can be analogized to the electrical equation $V = L\ddot{q}$, allowing force (F) to be mapped to voltage (V), mass (M) to inductance (L), and acceleration ($\ddot{y}$) to the second derivative of the charge ($\ddot{q}$). This approach is based on the analogous relationship from the mathematical form perspective between the governing equations of mechanical vibration systems and circuit systems, as outlined in the table below.

According to the lumped-parameter model described by equation (11) and the mechanical-electrical analogies summarized in Table 3, each physical quantity in the dynamic equations can be sequentially mapped to its corresponding circuit equivalent: the mass term corresponds to an inductance, the damping term to a resistance, and the stiffness term to a capacitance. Specifically, the bluff body displacement is analogous to the current in the circuit. Based on this mapping

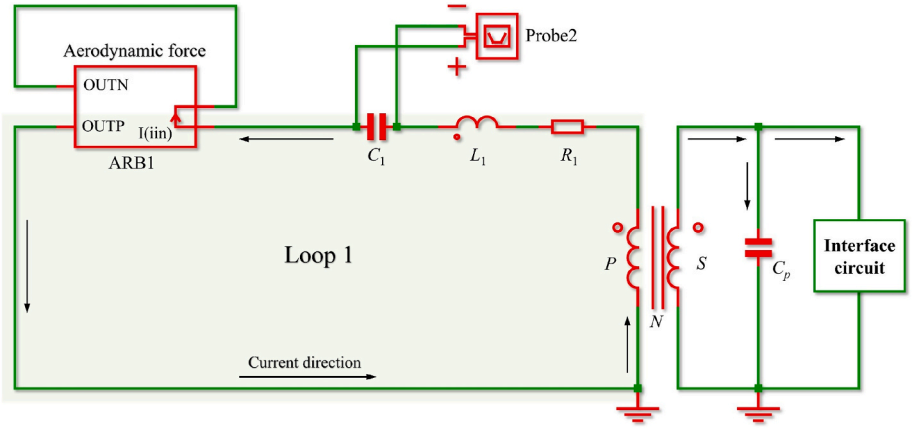

Fig. 11. The equivalent circuit model of the WGPEH.

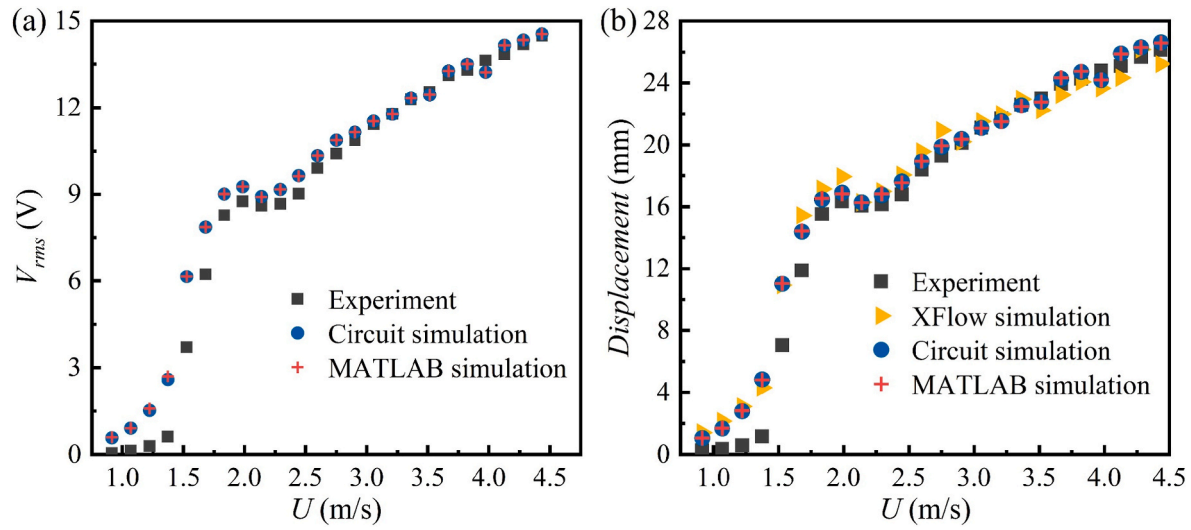

Fig. 12. The output response of the WGPEH versus wind speed obtained through experiments and different simulations: (a) The RMS open circuit voltage; (b) Tip displacement.

relationship, we can rewrite equation (11) into the form that describes a circuit involving LRC components as follows:

$$\begin{cases} L\ddot{q}(t)+R\dot{q}(t)+\dfrac{1}{C}q(t)+NV(t)=g_{01}\dot{q}(t)+g_{03}\dot{q}(t)^3+g_{05}\dot{q}(t)^5+\nu_{11}\sin(2\pi tS_{t1}U/D) \\ +\nu_{12}\cos(2\pi tS_{t1}U/D)+\nu_{21}\sin(2\pi tS_{t2}U/D)+\nu_{22}\cos(2\pi tS_{t2}U/D) \\ \dfrac{V(t)}{R_L}+C_p\dot{V}(t)-N\dot{y}(t)=0 \end{cases} \tag{12}$$

Furthermore, based on equation (12), we developed the equivalent circuit model in the SIMetrix environment, as shown in Fig. 11. Specifically, by systematically mapping each term in equation (12) to its corresponding circuit element using mechanical-electrical analogies and arranging them in appropriate series or parallel combinations, we constructed a complete circuit topology that faithfully replicates the structural dynamic response and piezoelectric transduction process.

The ARB1 block in Fig. 11 represents the aerodynamic force in the wake galloping model, which is given by the formula:

$$\text{ARB1} = -\left[\begin{array}{l} g_{01}I(iin)+g_{03}I(iin)^3+g_{05}I(iin)^5+\nu_{11}\sin(2\pi tS_{t1}U/D) \\ +\nu_{12}\cos(2\pi tS_{t1}U/D)+\nu_{21}\sin(2\pi tS_{t2}U/D)+\nu_{22}\cos(2\pi tS_{t2}U/D) \end{array}\right] \tag{13}$$

In the formula, $I(iin)$ is the current flowing through "loop 1", the current direction is shown in the figure, and the sign of the aerodynamic term is determined according to the current direction. Probe2 is the voltage probe used to measure the voltage across C_1, which can then be used to calculate the charge in loop 1, i.e., the displacement of the bluff body. By replacing the "interface circuit" in Fig. 11 with AC and DC circuits, the effects of different interface circuits on the WGPEH can be analyzed and studied in circuit simulation software.

4.3. Model validation

To fully determine the equivalent circuit model in Fig. 11, in addition to the system parameters listed in Table 1, it is also essential to acquire the following aerodynamic parameters: g_{01}, g_{03}, g_{05}, ν_{11}, ν_{12}, ν_{21}, and ν_{22}. Given the complex fluid-structure coupling effect involved in wake galloping, the aerodynamic force not only depends on the motion of the bluff body but also relates to the unsteady characteristics of the fluid. Therefore, predicting and modeling the aerodynamic force in wake galloping is more challenging than in VIV and galloping. The CFD model of the WGPEH has been presented and verified in Section 2.2. Based on CFD simulation results, MATLAB was used to fit the lift data F_y to identify the corresponding aerodynamic parameters. Given the complexity of the terms in equation (10), conventional curve fitting methods may fail to guarantee accuracy. This study uses the approach in Ref. [45] to identify the three aerodynamic damping coefficients and four vorticity component coefficients through a two-step process. The first step is to identify g_{01}, g_{03}, and g_{05}: Since the proportion of aerodynamic damping forces in F_{wg} is small, a strategy based on the energy equivalence principle is adopted to ensure the parameter identification accuracy. The first step involves aligning equation (10) with the work done by F_y at every time step. By utilizing known aerodynamic damping parameters and the downstream cylinder velocity $\dot{y}(t)$ extracted from CFD simulations, the first three terms of F_{wg} can be obtained and designated as F_{wg1}. The second step is to identify ν_{11}, ν_{12}, ν_{21}, and ν_{22}: The aerodynamic force F_y obtained from CFD was subtracted by F_{wg1} to yield the vortex-induced force, denoted as F_{wg2}. A least-squares fitting was then performed in MATLAB to identify the aerodynamic parameters.

Given a fixed distance ($L/D = 4$), aerodynamic characteristics are expected to be influenced solely by the structural shape and wind speed. As the structural configuration of the tandem cylinders remains unchanged throughout the investigation in this study, the aerodynamic parameters are primarily influenced by the wind speed. Thus, the aerodynamic parameters identified at different wind speeds can be plugged into equation (11), yielding a system of algebraic equations

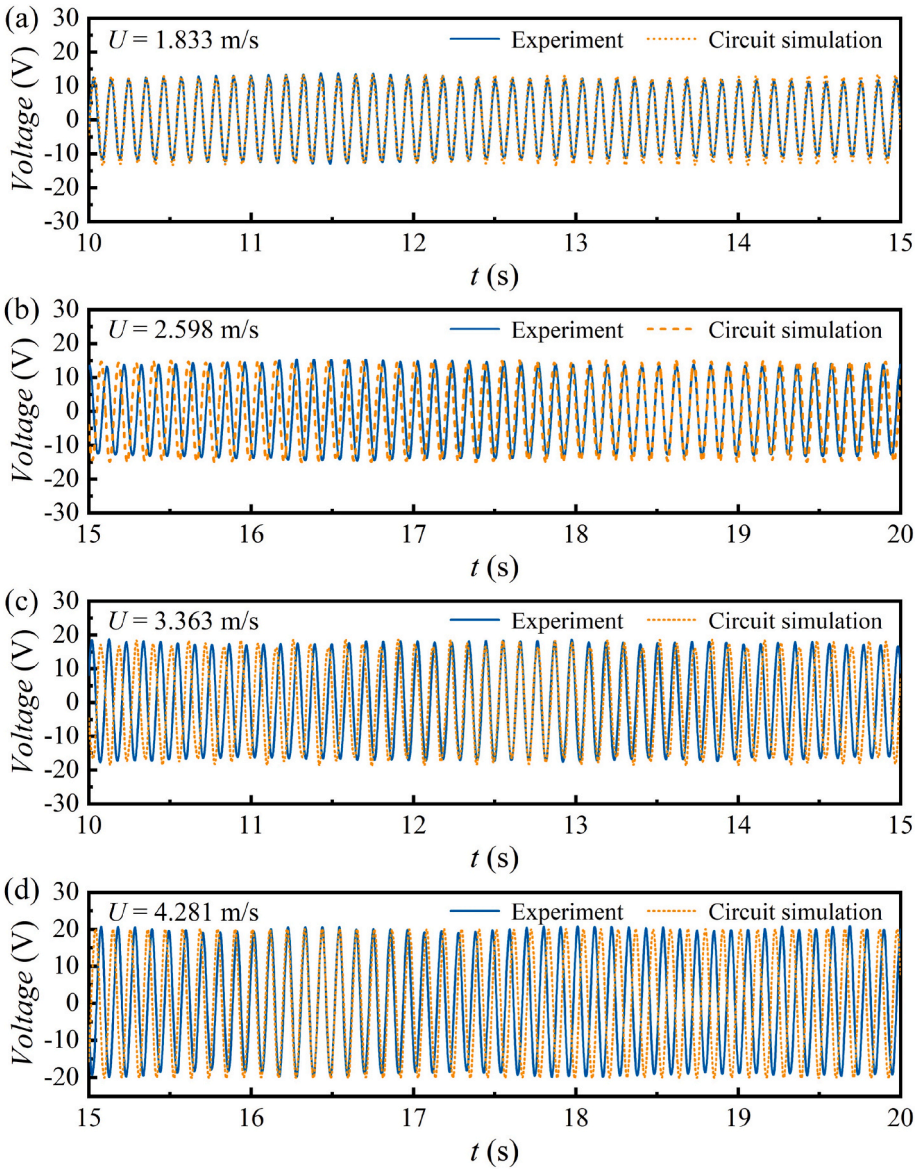

Fig. 13. For spacing ratio $L/D = 4$, the time history voltage responses at different wind speeds: (a) $U = 1.833$ m/s, (b) $U = 2.598$ m/s, (c) $U = 3.363$ m/s, (d) $U = 4.281$ m/s.

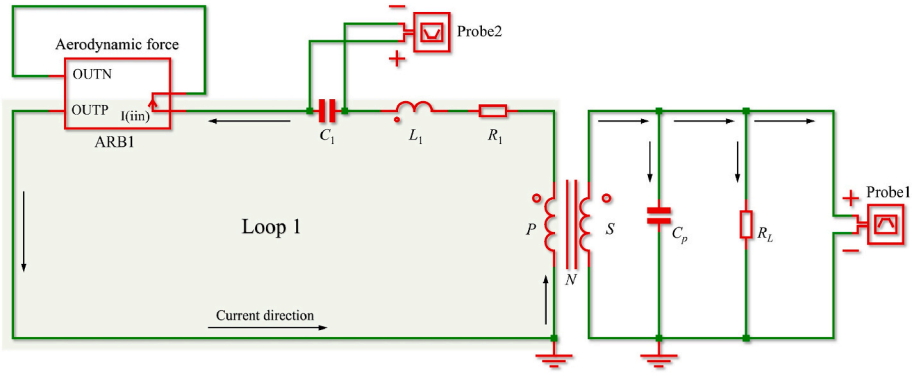

Fig. 14. The equivalent circuit model of the WGPEH shunted to an AC interface circuit.

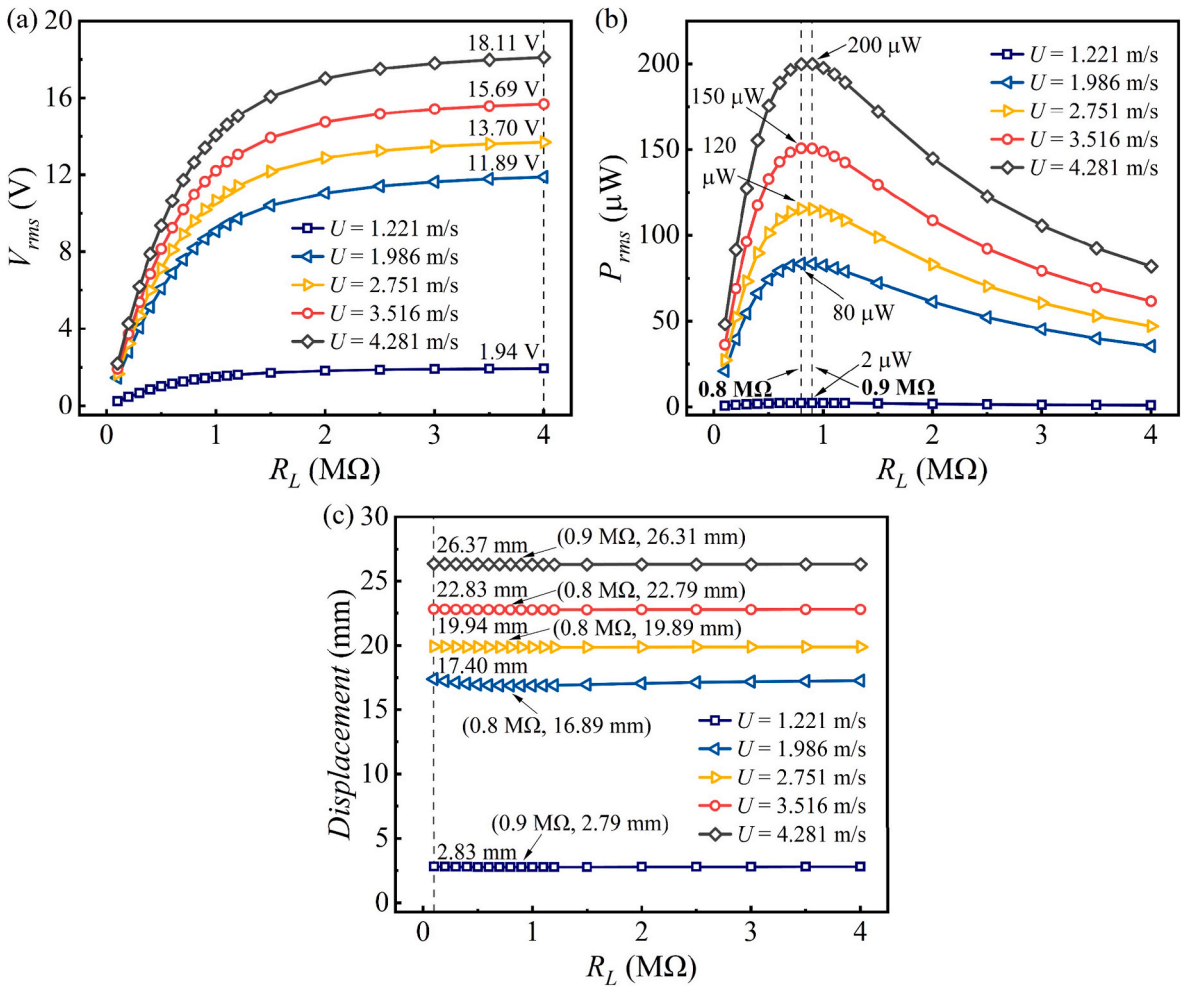

Fig. 15. Responses of the WGPEH shunted to an AC interface circuit at different load resistances: (a) RMS output voltage, (b) RMS output power, (c) displacement amplitude.

with two unknowns and two equations. The bluff body displacement and output voltage can then be obtained in two ways: first, by numerically solving equation (11) using the Runge-Kutta method in MATLAB (ode45 function); and second, by inputting the aerodynamic parameters into the "aerodynamic force" module shown in Fig. 11 in SIMetrix for transient analysis. Fig. 12 shows the responses of the WGPEH obtained through CFD simulation, the equivalent circuit method, the Runge-Kutta method, and experimental testing. The CFD simulation method cannot simulate voltage. Hence, XFlow simulation data is absent in Fig. 12(b). Compared with the experimental results, the maximum relative errors of the bluff body displacements obtained from CFD simulation, the ECM method, and the Runge-Kutta method are 10.55 %, 6.23 %, and 6.70 %, respectively, indicating that all three simulation models can effectively predict the output characteristics of the WGPEH. In particular, the ECM simulation results agree well with the Runge-Kutta results, with a maximum relative error of only 1.36 %. The observed deviation between simulation and experimental results at low wind speeds is primarily due to the cantilever beam used in the experimental setup. Positioned behind the bluff body, the beam acts as a passive splitter plate, disrupting near-wake vortex formation and weakening the aerodynamic excitation force. This leads to a slight reduction in vibration amplitude during experiments. In contrast, the CFD simulation does not include the cantilever beam, resulting in stronger vortex shedding and larger predicted amplitudes under the same conditions.

To further verify the accuracy of the circuit simulation, the voltage time-history curves obtained from the experiment and circuit simulation at the wind speeds 1.833 m/s, 2.598 m/s, 3.363 m/s, and 4.281 m/s are presented in Fig. 13. It can be found that the voltage amplitudes obtained from the circuit simulation and experiment testing are in excellent agreement across the four wind speeds.

5. Analyses of shunt circuits

Building on the research presented in the previous sections, we utilize the ECM of the WGPEH for system-level simulation. As the simplest interface circuit, the AC circuit is analyzed as a benchmark study. Since most electronic devices operate on DC power supplies, DC circuits are widely used in practical applications. Therefore, incorporating a DC circuit is crucial for accurately evaluating the performance of the PEH and assessing its energy conversion efficiency in real-world scenarios. In the following, we will analyze the performance of the WGPEH when connected to AC and DC interface circuits separately, followed by a comparison to highlight the key differences between the two.

5.1. AC interface circuit

The "interface circuit" in Fig. 11 is replaced with a pure resistor R_L, effectively shunting the WGPEH to an AC interface circuit, as depicted in Fig. 14. The voltage across R_L is monitored by a voltage probe, "Probe 1". The displacement is obtained by placing a probe "Probe 2" across the capacitor C_1 and then using the formula $q = C_1 V_{C1}$. The energy harvesting performance of the WGPEH can be studied by adjusting R_L to

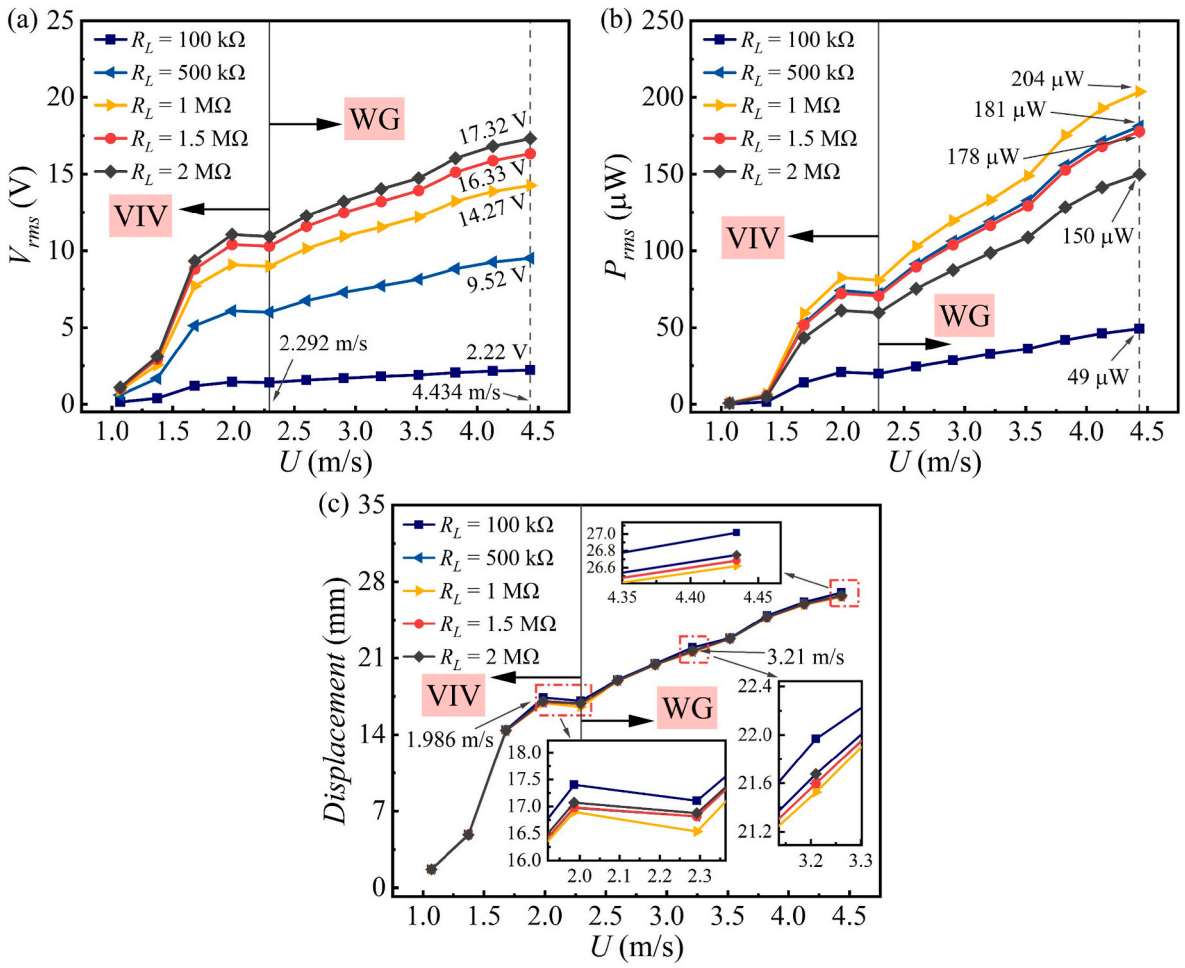

Fig. 16. Responses of the WGPEH shunted to an AC interface circuit at different wind speeds: (a) RMS output voltage, (b) RMS output power, (c) displacement amplitude.

explore various load conditions. In addition, the influence of wind speed on energy harvesting performance can be investigated by varying the aerodynamic parameters in ARB1.

Fig. 15 shows the RMS voltage, RMS power, and displacement of the WGPEH shunted to a resistor R_L under five different wind speed conditions. As shown in Fig. 15(a), the RMS voltage increases with R_L, though the increase rate gradually decreases. The RMS voltage tends to converge when the resistance is significantly large and can be deemed an open-circuit condition. Specifically, with $R_L = 4$ MΩ and the inlet wind speeds of 1.221 m/s, 1.986 m/s, 2.751 m/s, 3.516 m/s, and 4.281 m/s, the RMS voltage outputs are 1.94 V, 11.89 V, 13.70 V, 15.69 V and 18.11 V, respectively. In Fig. 15(b), the RMS power output first increases and then decreases with the increasing R_L. There is an optimal load (R_{opt}) to achieve the maximum power. However, the optimal load (R_{opt}) may vary at different wind speeds. At wind speeds of $U = 1.986$ m/s, 2.751 m/s, and 3.516 m/s, the WGPEH achieves peak power outputs with $R_{opt1} = 0.8$ MΩ, yielding power outputs of 80 μW, 120 μW and 150 μW, respectively. At wind speeds of $U = 1.221$ m/s and 4.281 m/s, the WGPEH attains maximum power outputs with $R_{opt2} = 0.9$ MΩ, producing power outputs of 2 μW and 200 μW, respectively.

Fig. 15(c) shows that the displacement of the bluff body is insensitive to the load resistance. At the five wind speeds of 1.221 m/s, 1.986 m/s, 2.751 m/s, 3.516 m/s, and 4.281 m/s, the maximum displacements of the energy harvester are obtained at 0.1 MΩ, measuring 2.83 mm, 17.40 mm, 19.94 mm, 22.83 mm, and 26.37 mm, respectively. The minimum displacement is achieved at the optimal load (R_{opt}) with increased electrical damping and reduced vibration of the bluff body. At wind speeds of 1.986m/s, 2.751 m/s, and 3.516 m/s, minimum displacements are observed at the optimal load resistance of 0.8 MΩ, measuring 16.89 mm, 19.89 mm, and 22.79 mm, respectively. When $U = 1.221$ m/s and 4.281 m/s, minimum displacements occur at $R_{opt2} = 0.9$ MΩ, measuring 2.79 mm and 26.31 mm, respectively. The disparities between the maximum and minimum displacements at the five wind speeds are 0.04 mm, 0.51 mm, 0.05 mm, 0.04 mm, and 0.06 mm, respectively. This suggests that the electrically induced damping of the WGPEH is most pronounced at a wind speed of 1.986 m/s.

Fig. 16 depicts the RMS voltage, RMS power, and displacement of the WGPEH versus the wind speed at the resistive loads of R_L is 100 kΩ, 500 kΩ, 1 MΩ, 1.5 MΩ, and 2 MΩ. The output response of the WGPEH exhibits characteristics of both VIV and WG. The critical wind speed is identified as 2.292 m/s: below this threshold, VIV dominates, while above it, WG prevails. For $U = 4.434$ m/s, the RMS voltage outputs of the WGPEH are 2.22 V, 9.52 V, 14.27 V, 16.33 V, and 17.32 V, respectively, at $R_L = 100$ kΩ, 500 kΩ, 1 MΩ, 1.5 MΩ, and 2 MΩ. For the WGPEH systems with R_L of 100 kΩ, 500 kΩ, 1 MΩ, 1.5 MΩ and 2 MΩ at a wind speed of 4.434 m/s, the RMS output power is recorded as 49 μW, 181 μW, 204 μW, 178 μW, and 150 μW, respectively. Fig. 16(c) shows the displacement variation in response to the wind speed. It can be seen that varying load resistances have minimal impact on the displacement responses at the same wind speed. Magnified views of the responses in three different ranges are provided. It evidently shows that the amplitude is largest when $R_L = 100$ kΩ and smallest when $R_L = 1$ MΩ.

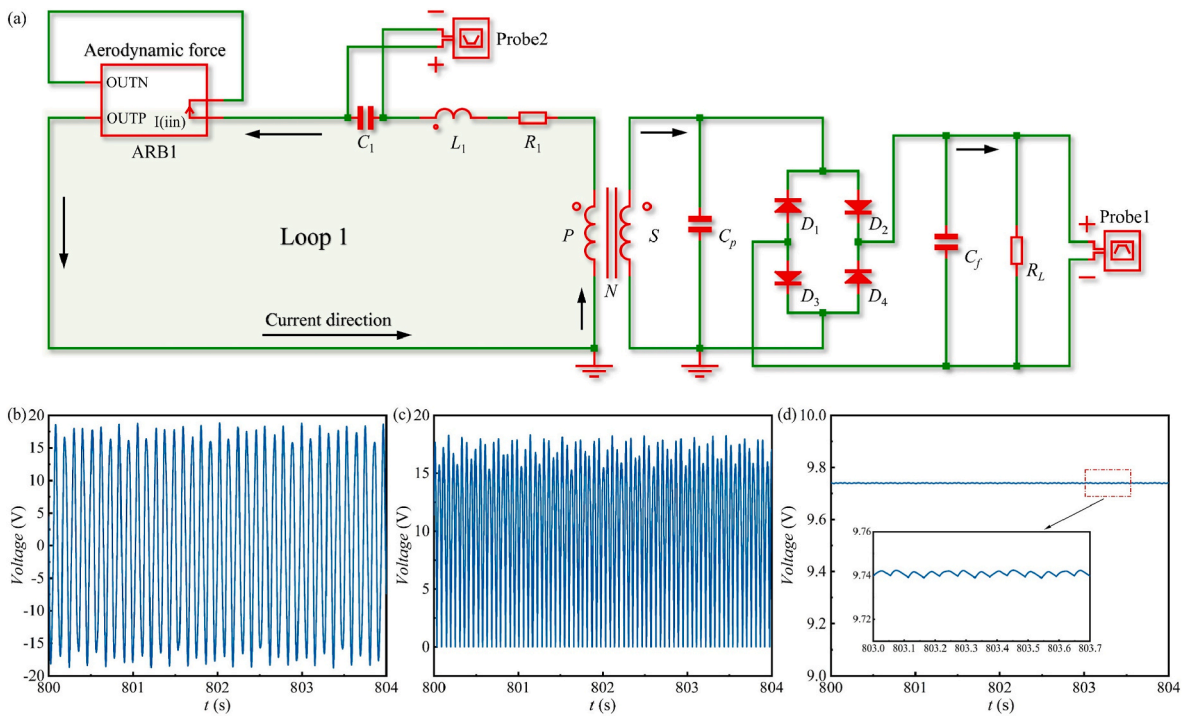

Fig. 17. (a) The equivalent circuit model of the WGPEH shunted to a DC circuit, (b) Time-history voltage output of the WGPEH, (c) Rectified voltage output, (d) Output voltage after connection to a filter capacitor.

5.2. DC interface circuit

The output produced by a PEH is in the form of AC power. Yet, most electronic devices necessitate direct current (DC) sources. Consequently, AC-DC rectification becomes crucial. Fig. 17 (a) illustrates the WGPEH shunted to a DC circuit. First, AC voltage is produced by the PEH, with the response curve shown in Fig. 17(b). Then, the AC voltage is rectified through a rectifier bridge composed of four diodes: D_1, D_2, D_3, and D_4, and the rectified response curve is shown in Fig. 17(c). Subsequently, a filter capacitor (C_f) is utilized to smooth out the DC output, resulting in a more steady DC voltage, as demonstrated in Fig. 17(d).

For the WGPEH with an AC interface circuit, it was found that when $U = 1.221$ m/s, the output response was too small compared to the other cases (Fig. 15(b)). To improve the visual presentation, the data for $U = 1.221$ m/s will be omitted, and the analysis will focus on comparing the cases of the remaining four operating conditions. The output response of the WGPEH shunted to a standard DC circuit is depicted in Fig. 18. As shown in Fig. 18(a), the RMS output voltage increases monotonically with the increase of the load resistance. Specifically, for $R_L = 4$ MΩ and the wind speed is 1.986 m/s, 2.751 m/s, 3.516 m/s, and 4.281 m/s, the generated voltages are 12.35 V, 14.37 V, 16.61 V, and 20.54 V, respectively. These output voltages of the WGPEH shunted to the DC circuit are higher than those observed under the same conditions but shunted to the AC circuit. From the data presented in Fig. 18(b), the average power initially rises before decreasing as the load resistance varies, suggesting an optimal load condition to achieve the maximum power output. Similar to the AC circuit interface, the energy harvester has the same $R_{opt} = 1.2$ MΩ at wind speeds of 1.986 m/s, 2.751 m/s, and 3.516 m/s. However, at the wind speed of 4.281 m/s, $R_{opt} = 1.5$ MΩ. The power outputs at these four wind speeds are 50 μW, 69 μW, 91 μW, and 139 μW, respectively. These values are lower than the optimal power outputs of the AC circuit interface at the same wind speeds, showing a reduction of 37.5 %, 42.5 %, 39.33 %, and 30.5 %, respectively. This power decrease is attributed to the voltage drops and power consumption in the diodes. Therefore, the AC circuit interface delivers more power at optimal load conditions than the DC circuit interface.

Under different wind speeds, Fig. 18(c) shows the change in the displacement of the bluff body when the DC load resistance changes. The results are similar to those of the one connected to the AC circuit, with peak displacement occurring at 0.1 MΩ and minimal displacement at the optimal load. For the DC interface circuit, the maximum displacements of the energy harvester at wind speeds of 1.986 m/s, 2.751 m/s, 3.516 m/s, and 4.281 m/s are 17.39 mm, 19.94 mm, 22.83 mm, and 26.36 mm, respectively. When comparing the displacements of the WGPEH connected to the AC interface circuit, the maximum difference in displacement is only 0.01 mm, suggesting almost no difference. The minimum displacements observed for the WGPEH shunted to the DC interface circuit are 17.12 mm, 19.91 mm, 22.80 mm, and 26.31 mm, respectively. Thus, the differences between maximum and minimum displacements are 0.27 mm, 0.03 mm, 0.03 mm, and 0.05 mm, respectively. Such differences are lower than the displacement differences observed for the AC circuit interface at the same wind speeds. The electrical damping effect reduces the vibration of the bluff body. The above results suggest that the electrical damping induced by the AC interface circuit is greater than that of the DC interface circuit at their corresponding optimal resistances.

When $R_L = 100$ kΩ, 500 kΩ, 1 MΩ, 1.5 MΩ, and 2 MΩ, the output response curve of the WGPEH with a DC interface circuit is shown in Fig. 19. Compared with the case of using an AC circuit, the output response trend of the WGPEH connected with DC has remained broadly consistent, exhibiting combined characteristics of VIV and WG. The critical wind speed is 2.292 m/s, but the amplitude has changed. As shown in Fig. 19(a), when $U = 4.434$ m/s, the WGPEH produces RMS voltages of 1.82 V, 7.09 V, 11.13 V, 13.74 V, and 15.58 V, respectively, at 100 kΩ, 500 kΩ, 1 MΩ, 1.5 MΩ, and 2 MΩ. All these values are lower than the outputs obtained when an AC interface circuit is used under the same conditions. As depicted in Fig. 19(b), with load resistances of 1 MΩ, 1.5 MΩ, and 2 MΩ, the RMS output power values at identical wind speeds show minimal variance, contrasting with the case when the AC circuit is utilized.

When $U = 4.434$ m/s, the RMS power outputs are 33 μW, 101 μW, 124 μW, 126 μW, and 121 μW, respectively. Compared with the WGPEH

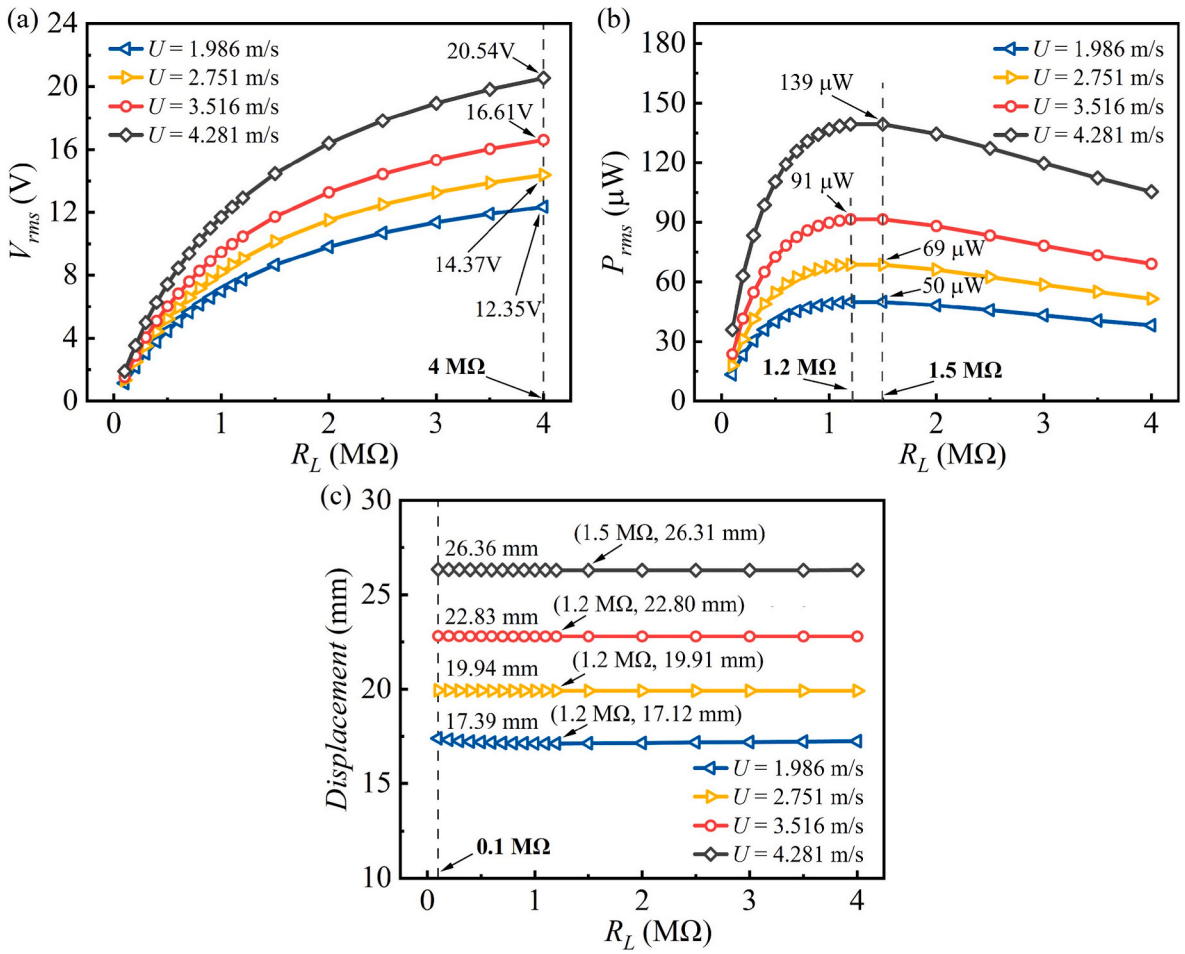

Fig. 18. Responses of the WGPEH shunted to a DC interface circuit at different load resistances: (a) RMS output voltage, (b) RMS output power, (c) displacement amplitude.

shunted to an AC circuit, the generated power under the same working conditions decreased by 32.65 %, 44.20 %, 39.22 %, 29.21 %, and 19.33 %, respectively. Fig. 19(c) shows the variation in the displacement of the bluff body at different wind speeds. One can note that varying load resistances have a minimal effect on the performance of the WGPEH shunted to the DC circuit at the same wind speed. In contrast, as shown in Fig. 16(c), the displacement changes under different load resistances are visually discernible at four wind speeds. The DC interface circuit has a relatively distinguishable difference only at two wind speeds of 1.986 m/s and 2.292 m/s. The magnified view in Fig. 19(c) shows that the amplitude is maximum when $R_L = 100$ kΩ and minimum when $R_L = 1.5$ MΩ.

6. Conclusion

This paper presents the study of a wake galloping piezoelectric energy harvester (WGPEH) consisting of tandem cylinders, and its equivalent circuit model is developed. Through system-level circuit simulations, the coupling behavior between the WGPEH under aerodynamic load and the complex interface circuit is assessed. First, the performance characteristics of the energy harvester under different spacing ratios are experimentally studied, and the CFD modeling analysis is carried out under the experimental condition of $L/D = 4$. The CFD simulation is validated by experimental results. Subsequently, the lift force, velocity, and displacement responses of the downstream cylinder, as obtained from the CFD simulation, are analyzed to characterize the aerodynamic forces involved in wake galloping. An equivalent circuit model (ECM) of the WGPEH is developed based on electromechanical analogies. By inputting identified aerodynamic parameters under different wind speeds into the circuit model, the output characteristics of the WGPEH can be predicted by circuit simulation. The simulation results exhibit a good agreement with the experimental ones. Finally, based on the ECM of the WGPEH, the effects of a DC interface circuit are investigated.

The key conclusions are outlined as follows: The experimental results show that at low wind speeds, the downstream cylinder is excited by vortex shedding from the upstream cylinder, exhibiting typical VIV. As the wind speed increases, the instability of the wake shear layer becomes more pronounced, leading to aerodynamic modulation and the development of negative aerodynamic damping. The system then enters a self-excited state, eventually resulting in large amplitude WG. In addition, due to the optimal matching between the wake disturbance and the dynamic response of the cylinder, there exists a spacing ratio to maximize energy harvesting efficiency. In this study, the best performance is observed at $L/D = 4$. The CFD flow field analysis reveals that the positive and negative vortices shed from the upstream cylinder become the input excitation of the downstream cylinder and interact with the downstream cylinder's shed vortices to grow, thus enhancing the downstream cylinder vibration and improving the energy harvesting efficiency. The experimental and simulation results show that the proposed equivalent circuit model of the WGPEH can predict the output responses of the WGPEH well and study the influences of practical interface circuits. Circuit simulations of the WGPEH shunted to different interface circuits indicate that the optimal load range of the AC circuit interface is 0.8–0.9 MΩ, while the DC circuit interface achieves the maximum output power in the range of 1.2–1.5 MΩ. Moreover, due to the voltage drops and

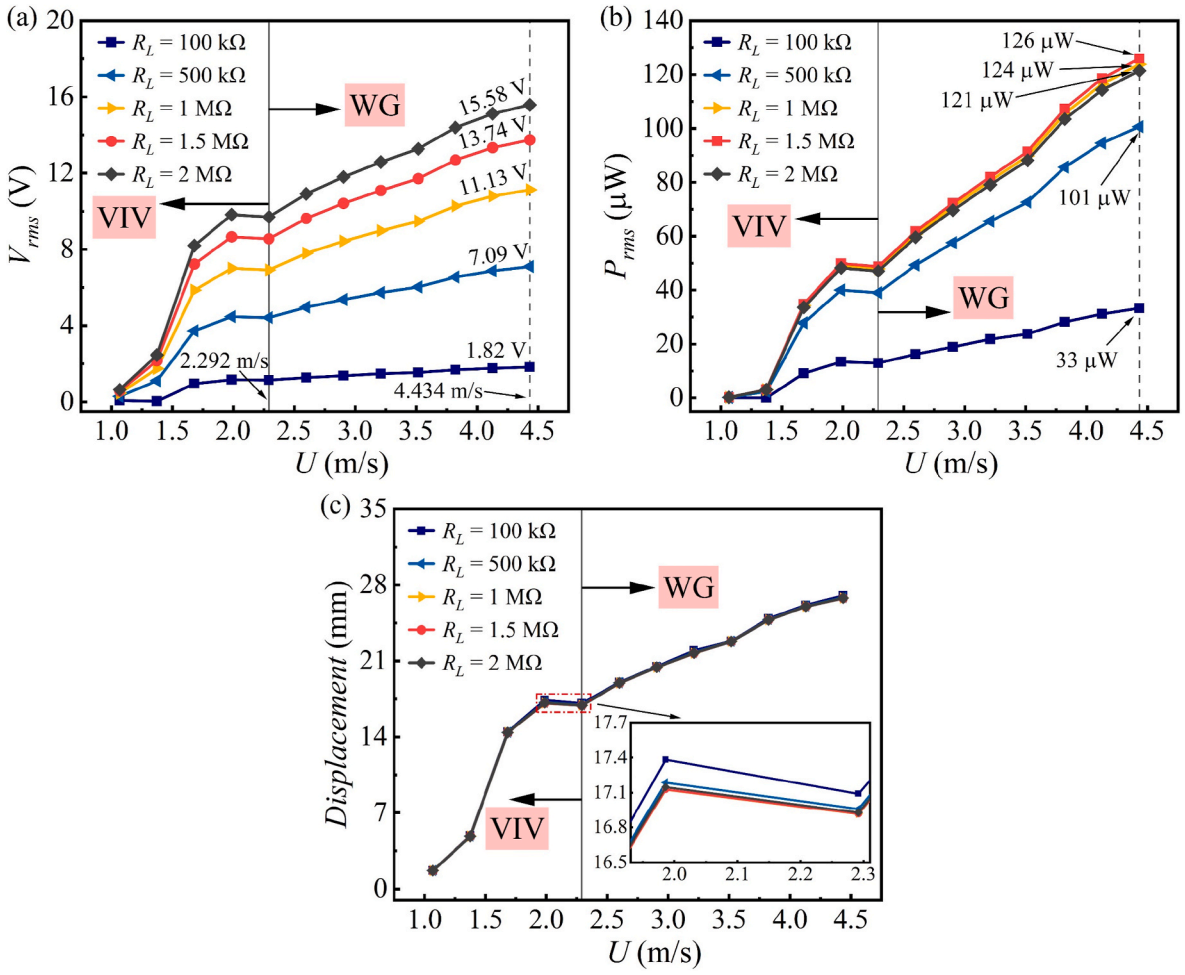

Fig. 19. Responses of the WGPEH shunted to a DC interface circuit at different wind speeds: (a) RMS output voltage, (b) RMS output power, (c) displacement amplitude.

power consumption of the rectifier bridge, the optimal output power of the DC circuit decreases by 42.5 % compared to the AC circuit. These findings offer a new perspective and approach for studying and applying wake galloping. In future work, more advanced interface circuits, such as SP-SSHI and SP-SECE circuits, can be integrated with the WGPEH for performance improvement.

CRediT authorship contribution statement

Junlei Wang: Writing – original draft, Validation, Resources, Investigation, Funding acquisition, Formal analysis, Conceptualization. **Liangjun Luo:** Writing – original draft, Visualization, Validation, Methodology, Investigation, Formal analysis, Data curation. **Ye Zhang:** Methodology, Investigation, Formal analysis, Data curation. **Guobiao Hu:** Writing – review & editing, Supervision, Project administration, Investigation, Funding acquisition, Formal analysis, Conceptualization.

Declaration of competing interest

The authors declare that they have no known competing financial interests or personal relationships that could have appeared to influence the work reported in this paper.

Acknowledgments

This work was financially supported by the National Natural Science Foundation of China (Grant Nos. 52277227, 52305135), Guangzhou Municipal Science and Technology Bureau (Grant Nos. SL2023A03J00869, SL2023A04J01741), Guangdong Provincial Project (2023QN10L545), and Guangzhou Municipal Key Laboratory on Future Networked Systems (Grant No. 024A03J0623).

Data availability

Data will be made available on request.

References

[1] Fang S, Du H, Yan T, Chen K, Li Z, Ma X, Lai Z, Zhou S. Theoretical and experimental investigation on the advantages of auxetic nonlinear vortex-induced vibration energy harvesting. Appl Energy 2024;356:122395.
[2] Wang J, Li P, Kang X, Li Z, Dai S. Soft-soft contact TENG using nonlinear coupling galloping phenomenon for harvesting wind energy. Nano Energy 2025;133:110471.
[3] Mehmood A, Abdelkefi A, Hajj MR, Nayfeh AH, Akhtar I, Nuhait AO. Piezoelectric energy harvesting from vortex-induced vibrations of circular cylinder. J Sound Vib 2013;332(19):4656–67.
[4] Sarviha A, Barati E. Piezoelectric energy harvester for scavenging steady internal flow energy: a numerical investigation. J Braz Soc Mech Sci Eng 2023;45(8):398.
[5] Tang L, Zhao L, Yang Y, Lefeuvre E. Equivalent circuit representation and analysis of galloping-based wind energy harvesting. IEEE ASME Trans Mechatron 2015;20:834–44.
[6] Wang J, Sun S, Hu G, Yang Y, Tang L, Li P, Zhang G. Exploring the potential benefits of using metasurface for galloping energy harvesting. Energy Convers Manag 2021;243:114414.
[7] Sarviha A, Barati E, Zarkak MR, Derakhshandeh JF, Alam MM. Experimental investigations on the wake-induced vibration of an electromagnetic energy-harvesting system. Int J Energy Res 2024;2024(1):7072340.

[8] Sarviha A, Barati E, Zarkak MR, Derakhshandeh JF, Alam MM, Zhang Z. Experimental investigations on the wake-induced vibration of an electromagnetic energy-harvesting system. Int J Energy Res 2024;2024(1):7072340.
[9] Bokaian A, Geoola F. Wake-induced galloping of two interfering circular cylinders. J Fluid Mech 2006;146:383–415.
[10] Dehkordi BG, Moghaddam HS, Jafari HH. Numerical simulation of flow over two circular cylinders in Tandem arrangement. J Hydrodyn 2011;23(1):114–26.
[11] Hishikar P, Dhiman SK, Tiwari AK, Gaba VK. Analysis of flow characteristics of two circular cylinders in cross-flow with varying reynolds number: a review. J Therm Anal Calorim 2021;147(10):5549–74.
[12] Dielen B, Ruscheweyh H. Mechanism of interference galloping of two identical circular cylinders in cross flow. J Wind Eng Ind Aerod 1995:289–300.
[13] Kim S, Kim H, Lee HC. An Experimental Investigation on Characteristics of Flow Field of Wake Galloping 2012.
[14] Hirano H, Maruoka A, Ikenouchi M. Numerical fluid flow analysis for aerodynamic response characteristics of Tandem circular cylinders. Int J Comput Fluid Dynam 1998;9(3–4):197–208.
[15] Adedeji BP. A multivariable output neural network approach for simulation of plug-in hybrid electric vehicle fuel consumption. Green Energy and Intelligent Transportation 2023;2(2):100070.
[16] Fang S, Wang X, Zhang X, Wu K, Yan T, Chuai X, Huang X, Li X, Lai Z, Dong S, Liao W-H. High output, lightweight and small-scale rotational piezoelectric energy harvester utilizing internal impact effect. Energy Convers Manag 2024;322:119180.
[17] Yan M, Xu H, Li M, He H, Bai Y. Hierarchical predictive energy management strategy for fuel cell buses entering bus stops scenario. Green Energy Intell Transp 2023;2(4):100095.
[18] Hu G, Tang L, Das R. An impact-engaged two-degrees-of-freedom Piezoelectric energy harvester for wideband operation. Procedia Eng 2017;173:1463–70.
[19] Tian H, Shan X, Cao H, Song R, Xie T. A method for investigating aerodynamic load models of piezoaeroelastic energy harvester. J Sound Vib 2021;502:116084.
[20] Wang J, Han C, Jo S-H, Xu W, Tian H. Enhanced flow induced vibration piezoelectric energy harvesting performance by optimizing tapered beam. Ocean Eng 2024;300:117459.
[21] Fang S, Chen K, Lai Z, Zhou S, Yurchenko D, Liao W-H. A bio-inspired system for simultaneous vibration isolation and energy harvesting in post-capture spacecraft. Mech Syst Signal Process 2023;199:110466.
[22] Fang S, Peng H, Zhang C, Lai Z, Zhou S, Zhu R, Liao W-H, Inman DJ. Synchronous and asynchronous vibration suppression and energy harvesting techniques: principles, methods and applications. Eng Struct 2024;321:118994.
[23] Xia B, Mei X, Wang J. Enhanced performance of piezoelectric energy harvester by installing symmetrical flexible splitter plates. Mech Syst Signal Process 2025;225:112257.
[24] Wang J, Han C, Yurchenko D, Zhou Y, Meng X, Zhang W. Energy concentration pipe based on passive jet control for enhancing flow induced vibration energy harvesting. Energy Convers Manag 2024;319:118948.
[25] Wang J, Sun Z, Hu G, Ding H, Li X. Improving mechanical energy harvesters without complex fabrication using origami/kirigami. Device 2024;2(9):100548.
[26] Wang J-l, Li S-f, Alam MM, Zhu H-j, Hu G-b. Energy harvesting in the wake of an inverted C-Shaped bluff body. China Ocean Eng 2024;38(1):68–80.
[27] Tao K, Yi H, Yang Y, Chang H, Wu J, Tang L, Yang Z, Wang N, Hu L, Fu Y, Miao J, Yuan W. Origami-inspired electret-based triboelectric generator for biomechanical and ocean wave energy harvesting. Nano Energy 2020;67:104197.
[28] Usman M, Hanif A, Kim I-H, Jung H-J. Experimental validation of a novel piezoelectric energy harvesting system employing wake galloping phenomenon for a broad wind spectrum. Energy 2018;153:882–9.
[29] Zhao D, Zhou J, Tan T, Yan Z, Sun W, Yin J, Zhang W. Hydrokinetic piezoelectric energy harvesting by wake induced vibration. Energy 2021;220:119722.
[30] Jung H-J, Lee S-W. The experimental validation of a new energy harvesting system based on the wake galloping phenomenon. Smart Mater Struct 2011;20(5):055022.
[31] Du X, Chen H, Li C, Li Z, Wang W, Guo D, Yu H, Wang J, Tang L. Wake galloping piezoelectric-electromagnetic hybrid ocean wave energy harvesting with oscillating water column. Appl Energy 2024;353:122081.
[32] Liu Y, Liu J, Xue K, Seok J. Development of a novel wake-induced rotational galloping wind energy harvester and the identification of its working mechanism. Mech Syst Signal Process 2025;224:112019.
[33] Tao K, Tang L, Wu J, Lye SW, Chang H, Miao J. Investigation of multimodal electret-based MEMS energy harvester with impact-induced nonlinearity. J Microelectromech Syst 2018;27(2):276–88.
[34] Liang J, Liao W-H. Improved design and analysis of self-powered synchronized switch interface circuit for piezoelectric energy harvesting systems. IEEE Trans Ind Electron 2012;59(4):1950–60.
[35] Liang J, Liao W-H. Impedance modeling and analysis for piezoelectric energy harvesting systems. IEEE ASME Trans Mechatron 2012;17(6):1145–57.
[36] Wang L, Tan T, Yan Z, Li D, Zhang B, Yan Z. Integration of tapered beam and four direct-current circuits for enhanced energy harvesting from transverse galloping. IEEE ASME Trans Mechatron 2019;24(5):2248–60.
[37] Yang Y, Tang L. Equivalent circuit modeling of piezoelectric energy harvesters. J Intell Mater Syst Struct 2009;20(18):2223–35.
[38] Priore ED, Romano GP, Lampani L. Coupled electro-aeroelastic energy harvester model based on piezoelectric transducers, VIV-Galloping interaction and nonlinear switching circuits. Smart Mater Struct 2023;32(7):075012.
[39] Zhao L, Tang L, Liang J, Yang Y. Synergy of wind energy harvesting and synchronized switch harvesting interface circuit. IEEE ASME Trans Mechatron 2017;22(2):1093–103.
[40] Zhao L, Yang Y. Analytical solutions for galloping-based piezoelectric energy harvesters with various interfacing circuits. Smart Mater Struct 2015;24(7):075023.
[41] Zhao L, Yang Y. Comparison of four electrical interfacing circuits in wind energy harvesting. Sensor Actuator Phys 2017;261:117–29.
[42] Jia JD, Shan XB, Zhang XX, Xie T, Yang YW. Equivalent circuit modeling and analysis of aerodynamic vortex-induced piezoelectric energy harvesting. Smart Mater Struct 2022;31(3):035009.
[43] Wang J, Luo L, Yurchenko D, Hu G. Equivalent circuit analysis of a nonlinear vortex-induced vibration piezoelectric energy harvester using synchronized switch technique. IEEE Trans Ind Electron 2024:1–12.
[44] Abdelkefi A, Scanlon JM, McDowell E, Hajj MR. Performance enhancement of piezoelectric energy harvesters from wake galloping. Appl Phys Lett 2013;103(3):033903.
[45] Yang X, Yan Z, Fu H, Wang L, Savory E. Nonlinear modelling of unsteady wake galloping forces on a circular cylinder in the wake of a fixed cylinder. Ocean Eng 2022;250:111016.
[46] Assi GRS, Bearman PW, Meneghini JR. On the wake-induced vibration of tandem circular cylinders: the vortex interaction excitation mechanism. J Fluid Mech 2010;661:365–401.
[47] Hover FS, Triantafyllou MS. Galloping response of a cylinder with upstream wake interference. J Fluid Struct 2001;15:503–12.
[48] Hu Z, Wang J, Sun Y. Flow-induced vibration of one-fixed-one-free tandem arrangement cylinders with different mass-damping ratios using wind tunnel experiment. J Fluid Struct 2020;96:103019.
[49] Assi GRS. Wake-induced vibration of tandem and staggered cylinders with two degrees of freedom. J Fluid Struct 2014;50:340–57.
[50] Yuan P, Schaefer L. Equations of state in a lattice Boltzmann model. Phys Fluids 2006;18(4):042101.
[51] Zhu H, Zhong J, Liu B. Fluid–thermal–structure interaction of three heated circular cylinders in tandem at a low Reynolds number of 150. Phys Fluids 2022;34(8):083605.
[52] Lee C-M, Paik K-J, Kim ES, Lee I. A fluid–structure interaction simulation on the wake-induced vibration of tandem cylinders with pivoted rotational motion. Phys Fluids 2021;33(4):045107.
[53] Zeng LW, Zhao FW, Wang HF, Liu Y, Tang H. Control of flow-induced vibration of a circular cylinder using a splitter plate. Phys Fluids 2023;35(8):087104.
[54] Hu G, Tang L, Liang J, Das R. Modelling of a cantilevered energy harvester with partial piezoelectric coverage and shunted to practical interface circuits. J Intell Mater Syst Struct 2019;30(13):1896–912.
[55] Hu G, Wang J, Tang L. A comb-like beam based piezoelectric system for galloping energy harvesting. Mech Syst Signal Process 2021;150:107301.
[56] Jia J, Shan X, Zhang X, Xie T, Yang Y. Equivalent circuit modeling and analysis of aerodynamic vortex-induced piezoelectric energy harvesting. Smart Mater Struct 2022;31(3):035009.
[57] Hoseyni SM, Aghakhani A, Basdogan I. Experimental admittance-based system identification for equivalent circuit modeling of piezoelectric energy harvesters on a plate. Mech Syst Signal Process 2024;208:111016.
[58] Tang L, Yang Y. A nonlinear piezoelectric energy harvester with magnetic oscillator. Appl Phys Lett 2012;101(9):094102.
[59] Gao GZ, Zhu LD. Nonlinear mathematical model of unsteady galloping force on a rectangular 2:1 cylinder. J Fluid Struct 2017;70:47–71.
[60] Yang X, Yan Z, Fu H, Wang L, Savory E. Nonlinear modelling of unsteady wake galloping forces on a circular cylinder in the wake of a fixed cylinder. Ocean Eng 2022;250:111016.
[61] Fu H. Unsteady aerodynamic force model and behavior of wake galloping for a downstream circular cylinder in tandem (master dissertation). Chongqing University, China; 2020.